

1 Microscopic and geochemical analyses of the Tonian
2 Longfengshan biota from the Luotuoling Formation (Hebei
3 Province, North China) with taphonomic implications

4
5 Yinghao Jing¹, Zhong-Qiang Chen^{1,*}, Ross P. Anderson^{2,3}, Xue Wang¹, Zemin Zheng¹,
6 Xueqian Feng¹

7
8 ¹ State Key Laboratory of Biogeology and Environmental Geology, China University
9 of Geosciences (Wuhan), Wuhan, 430074, China

10 ² All Souls College, University of Oxford, Oxford OX1 4AL, UK

11 ³ Department of Earth Sciences, University of Oxford, Oxford OX1 3AN, UK

12
13 *Corresponding author. E-mail address: zhong.qiang.chen@cug.edu.cn
14

15 **Abstract**

16 The Tonian Longfengshan biota is among the earliest known fossil assemblages with a
17 predominance of the benthic macroalgal fossil *Longfengshania* Du, 1982, which is well
18 known for its blade, stipe, and holdfast differentiation. However, the microstructure and
19 geochemical composition of these fossils are poorly understood. We documented the
20 microscopic characteristics, mineralogy, and geochemistry of 29 fossil specimens from
21 the Luotuoling Formation at the Longfengshan locality of Hebei Province, North China
22 using scanning electron microscopy (SEM), energy dispersive X-ray spectrometry
23 (EDS), micro X-ray fluorescence spectroscopy (μ -XRF), Raman spectroscopy, and X-
24 ray Diffraction (XRD). SEM-EDS revealed that all fossil specimens are preserved as
25 two-dimensional compressions that are composed of carbonaceous patches and also
26 have high calcium content. Iron-rich clay minerals were additionally detected in
27 association with the fossils. μ -XRF mapping confirmed the fossils' high calcium
28 content. Raman spectroscopy showed that carbonaceous patches are comprised of
29 disordered organic carbon that has been altered by low grade metamorphism (< 300 °C).

XRD showed a homogenous mineralogy (dominated by quartz, feldspar, and muscovite with other minor e.g., kaolinite, smectite). Petrographic analysis revealed that microbial mats existed in the fossil-bearing shale, implying that benthic macroalga *Longfengshania* attached its holdfast in a sticky microbial mat that encrusted the seabed. Integration of these data suggested that the fossil-bearing silty shale was deposited in the subtidal zone below storm wave base. Iron-replete but sulfate-depleted porewater within sediments may have inhibited the degradation process of the Longfengshan macroalgae.

Keywords: complex life, Neoproterozoic Era, macroalgae, soft-tissue fossilization, iron-rich clay minerals.

1. Introduction

The early Neoproterozoic Tonian Period (1000–720 Ma) witnessed significant changes in environment and considerable biotic evolution at the dawn of complex eukaryotic life on our planet (Lyons et al., 2014; Xiao and Tang, 2018; Cohen and Kodner, 2022). During this time, the taxonomic diversity, morphospace range, and morphological disparity of benthic macroalgae increased significantly (Xiao and Dong, 2006; Cohen and Macdonald, 2015; Xiao and Tang, 2018; Bykova et al., 2020; Tang et al., 2020). Most macroalgae are preserved in marine fine-grained sediments (i.e., shales) as carbonaceous compressions, and may share a similar taphonomic mechanism to fossils from iconic Cambrian/Ordovician deposits with Burgess Shale-type (BST) preservation. Previous studies on the taphonomic mode of carbonaceous compression fossils are largely confined to these Cambrian/Ordovician exceptionally preserved biotas (e.g., Butterfield, 1990, 1995; Orr et al., 1998; Gabbott et al., 2004; Zhu et al., 2005; Gaines et al., 2008, 2012; Forchielli et al., 2014; Gaines, 2014; Anderson et al., 2018, 2021; Saleh et al., 2019). Few studies have investigated the taphonomy of older carbonaceous compressions (e.g., Anderson et al., 2011; Wacey et al., 2014; Anderson et al., 2020; Becker-Kerber et al., 2022; Maloney et al., 2022). The Tonian

Longfengshan biota of North China, dominated by carbonaceous compressions of macroalgal fossils, provides the opportunity for new insights into the taphonomy of carbonaceous compressions in such older strata.

The Tonian Longfengshan biota is dominated by the macroalgae *Longfengshania* Du, 1982, *Tawuia* Hofmann, 1979, and *Chuarina* Walcott, 1899 (Du and Tian, 1985, 1986; Du et al., 2009; Liu, 2018). All these macroalgae are preserved as carbonaceous compressions on bedding surfaces of silty shales. *Longfengshania* is anatomically most interesting, being characterized by blade, stipe, and holdfast differentiation, and has been interpreted to be benthic and sessile (Du and Tian, 1985, 1986). The stipe and holdfast of *Longfengshania* suggest it may have been one of the first eukaryotic fossil organisms recorded to attach to the seabed and grow vertically away from the substratum and closer to the light, like its modern marine analogues (Hurd et al., 2014). As a result, the Longfengshan biota, especially *Longfengshania*, has received intensive attention from paleobiologists over the last four decades. However, most studies have focused on gross fossil morphology and few studies have examined its internal microstructure, and elemental and mineral compositions, or how it was preserved.

To investigate the microstructure, elemental and mineral composition, and the taphonomy of the Longfengshan biota, we carried out detailed petrographic observations on the fossil-bearing strata and macroalgal fossils, and deployed a combination of microanalytical techniques: optical microscopy, scanning electron microscopy (SEM), energy dispersive X-ray spectroscopy (EDS), micro-X-ray fluorescence spectroscopy (μ -XRF), Raman micro-spectroscopy, and selected-area *in situ* X-ray diffraction (XRD). The biota was investigated at the iconic Longfengshan locality of the Luotuling Formation in Hebei Province, North China (Fig.1). This study provides a better understanding of the taphonomic processes involved in the fossilization of Tonian macroalgae, with emphasis on the environmental controls that may have contributed to the preservation of carbonaceous compressions.

2. Geological context

Macroalgal fossils were collected from the Longfengshan locality (40°28'56"N, 115°26'57"E) of Huailai County, Hebei Province, North China (Fig. 1; Du and Tian, 1985). The Huailai area is located in the northern part of the North China Craton (Fig. 1A–B). In this area, the Tonian succession of silty shale, siltstone, and sandstone is assigned to the Luotuoling Formation, which unconformably overlies the Mesoproterozoic Xiamaling Formation and is also unconformably overlain by Tonian deposits of the Jingeryu Formation (Figs. 1C, 2A–B; Du et al., 2009; Jin et al., 2020).

In the Longfengshan section, the Luotuoling Formation is further subdivided into 34 layers that are categorized into two members, with a total thickness of ca. 70 m (Fig. 1C; Du and Tian, 1986; Du et al., 2009; Liu, 2018). Member I is mainly composed of glauconite quartz sandstone with a coarse conglomerate at its base. Herringbone cross-bedding is pronounced in the lower part of Member I (Fig. 2D), pointing to a tidal environment. Member II is characterized by two shale units interbedded with a sandstone layer in the lower part, and glauconite quartz sandstone in the upper part (Fig. 1C). The upper shale unit in the lower part of Member II is silty and yields abundant macroalgal fossils (Figs. 1C, 2G–K). The fining-up succession of siltstone and sandstone observed in Member I to the laminated black shales of the lower part of Member II suggests transitions in facies from fluvial to nearshore and then to offshore settings, which, overall, exhibit an increase in water depth. The reoccurrence of coarse-grained sandstones in the middle and upper parts of Member II indicates a relatively high-energy environment in a shallow marine setting.

The Luotuoling Formation is traditionally assigned to the Qingbaikou Group which was deposited in the Tonian Period (Halverson et al., 2020). As a result, the Luotuoling Formation and the Longfengshan biota are broadly constrained as Tonian (1000–720 Ma) in age. This temporal correlation is reinforced by correlations of stratigraphic successions within the North China Craton and fossil assemblages with their counterparts elsewhere in the world (Du et al., 2009; Wang et al., 2021). For example, the *Longfengshania-Chuaria-Tawuia* fossil assemblage of the Luotuoling Formation is comparable to the assemblage reported from the Tonian Little Dal Group of northwestern Canada (Hofmann, 1985).

3. Material and methods

3.1. Material

Macroalgal fossil specimens were collected from the silty shale of layer 22 in the lower part of Member II of the Luotuoling Formation at the Longfengshan locality (Fig. 1C). The host silty shale is well laminated, is comprised of a series of repeatedly varying mm-scale dark-light laminae couplets, and in places its bedding surfaces have been weathered to a rusty reddish color (Fig. 2G–H). The fossil horizon, a continuous interval, about 2 m thick, was sampled following extensive excavation and subjected to high-resolution bed-by-bed sedimentological analysis (Fig. 2G). A representative selection of the lithological samples was prepared as cross-sections and polished transverse slabs for fine-scale examination of sedimentary structures and petrographic textures. During the excavation, ~100 fossil-bearing rock slabs were collected. Some slabs have multiple specimens on their bedding surfaces, and others were split to produce a part and counterpart of fossils (Fig. 2I–K). A total of 29 fossil specimens were analyzed using the techniques described below (twelve specimens of *Longfengshania*, six of *Tawuia*, and five of *Chuarua*, the other six specimens are incomplete and are tentatively assigned to either *Tawuia* or *Longfengshania*, Fig. 3).

3.2. Optical microscopy

All fossil specimens were photographed using a Canon digital SLR camera, and then examined under reflected light using a Zeiss Axio scope A1 microscope coupled with an Axiocam 506 color CCD detector at Biogeology and Environmental Geology (BGEG), China University of Geosciences (Wuhan) in Wuhan, China. Photomicrographs of fossils were taken at different focal planes and combined using Adobe Photoshop to create a “Z-stack” composite image. Petrographic studies of fossil-bearing layers were carried out on cross sections using the Zeiss Axio scope A1

microscope system under transmitted light.

3.3. Scanning electron microscopy (SEM), energy dispersive X-ray spectroscopy (EDS), and micro X-ray fluorescence spectroscopy (μ -XRF)

A total of 16 fossil specimens were examined using a Hitach SU8010 field-emission scanning electron microscope equipped with an Oxford Instruments energy dispersive X-ray spectrometer at BGEG. The samples were coated with a 2-nm-thick Pt veneer for electric conduction (see also Fang et al., 2017; Wu et al., 2017).

EDS element mapping of fossil individuals was employed to document elemental distributions across fossil surfaces and surrounding matrix. All EDS analyses were performed using accelerating voltages of 15–25 KV, a working distance of ~ 15 mm, and an electron beam current of 10 nA (Chen et al., 2014; Jing et al., 2022). Since topographic variation may bias element mapping (Cai et al., 2012; Meyer et al., 2012), point EDS analyses were also carried out on flat areas of the fossils and their surrounding matrices separately ($n = 335$; $n_{\text{fossil}} = 178$, $n_{\text{matrix}} = 157$). All elemental point data herein are reported in mean normalized weight percentages (nwp).

In addition, a large fossil-bearing slab was selected for element mapping using μ -XRF. The sample was uncoated and element mapping was performed using a M4 Tornado μ -XRF (Bruker, Germany) at Buoyue Instruments Co. Ltd in Shanghai, China. The accelerating voltage and beam current were 50 kV and 600 μ A, respectively.

3.4. Selected-Area in situ X-ray Diffraction (XRD)

In situ XRD was performed over selected areas of 1×7 mm on fossil surfaces and their surrounding matrix to determine their mineralogical composition at the Department of Earth Sciences, University of Oxford in Oxford, UK. The analytical procedure follows Anderson et al. (2021).

3.5. Raman micro-spectroscopy

To document the chemical structure of carbonaceous material within fossils, Raman spectra were obtained using a WiTec alpha 300 Confocal Raman laser microscope with a 532-nm wavelength laser and operating at a power 1 mW under reflected light at BGEG. The analytical procedure follows Yang et al. (2022).

4. Results

4.1. Petrography of fossil-bearing strata

Microscopically, the fossil horizon is generally well laminated and comprises alternations of dark and light laminae couplets (Fig. 4A–C). It is notable that the fossils are most abundant in the dark clay-rich laminae. These laminae are carbonaceous and characterized by irregularly undulating microbial mats. In contrast, the light laminae comprise fine-grained detrital quartz and clasts of mat chips (Fig. 4D–F). At the dark-light interface, erosional bases with sand-sized grains and microscours usually develop, forming soft-sediment deformation structures as load casts (Fig. 4A–B, 4G).

Within both the dark and light laminae, aggregated spherical minerals bearing framboidal textures are abundant, often “floating” in the matrix (Fig. 4H–J). Using SEM, these framboids exhibit numerous aggregated rosettes of platelets enclosed by a thick crust (Fig. 4K–O). Void structures in these minerals are also documented where the infillings are removed (Fig. 4K, M). Framboids consisting of euhedral crystals can also be identified with SEM but are rare (Fig. 4P–Q).

4.2. Macroscopic and microscopic characteristics of macroalgae fossils

Macroalgal fossils are preserved as two-dimensional carbonaceous compressions on bedding planes. Fossils can either be only sporadically present or densely distributed on bedding surfaces (Fig. 2I–J). In the latter case, macroalgal fossils are randomly orientated (Fig. 2J). These carbonaceous compression fossils are easily distinguished

from the surrounding rocks due to their dark color (Fig. 2I–J). Three genera represent the majority of fossils: *Longfengshania*, *Tawuia*, and *Chuarua* (Fig. 3). *Longfengshania* is characterized by blade, stipe, and holdfast differentiation. The blade and stipe are conspicuous in the specimens, while no complete holdfasts are recognized in our collection. The *Longfengshania* individuals include various morphotypes, including lollipop-shaped, tadpole-shaped, and leaf-shaped forms (Fig. 3A). *Tawuia* is usually oval in outline (Fig. 3B), and *Chuarua* is round in shape (Fig. 3C). In general, all fossils are flat and smooth, with some individuals showing minor folds, suggesting some degree of flexibility of the original organic materials. Some individuals have nearly concentric wrinkles along their margins (Fig. 3), implying that their original shape of the organism/blade could have been spherical.

Light microscopy (LM) in reflected light revealed that the macroalgal fossils consist of highly reflective carbonaceous patches (Figs. 5A–E, 6A–B). These carbonaceous patches are irregular in shape and scattered. The margins of the patches are polygonal and seem to match to adjacent patches such that they fit together well with their corners showing angular junctions (Figs. 5E, 6B). Therefore, the patchiness of the carbonaceous material across each fossil is probably due to dehydration during fossilization. The carbonaceous patches are even more pronounced using SEM (Figs. 5F–H, 6I–J, 7). They reach dozens of micrometers in diameter and are ~1 μm in thickness.

Fossil preservation is closely related to the degree of weathering. Fossils preserved on weathered bedding surfaces appear rusty orange in color (Figs. 5A–B, 7G, 7M), and preserve few carbonaceous patches, while fossils occurring on the un-weathered bedding surfaces are darker in color and contain a greater amount of carbonaceous patches (Figs. 6A, 7A).

4.3. Element compositions of fossils and their surrounding matrix

EDS revealed that the elements C, O, Mg, Al, Si, S, K, Ca, Ti, and Fe generally define the composition of both fossils and surrounding matrices. EDS point analyses of

eight fossil specimens showed that their elemental constituents include: C = 43.8%, O = 18.3%, Mg = 0.7%, Al = 6.1%, Si = 16.4%, S = 0.5%, K = 4.7%, Ca = 3.0%, Ti = 1.0%. Fe = 5.5% (in mean nwp, n = 178, Table 1). Elemental constituents of the surrounding matrix are: C = 5.0%, O = 31.3%, Mg = 0.8%, Al = 13.3%, Si = 31.3%, S = 0.3%, K = 8.7%, Ca = 0.3%, Ti = 1.2%. Fe = 8.0% (in mean nwp, n = 157, Table 1). Point data showed that the elements C and Ca are more abundant in fossils than that in their surrounding matrix (Fig. 8A). However, the elements O, Al, Si, K, and Fe are lower in abundance in fossils *versus* matrix (Fig. 8A). The concentrations of the elements Mg, S, and Ti in both fossils and matrix are very low (<3%). Among them, the elements Mg and Ti do not show obvious bias to fossils *versus* matrix, while S is slightly higher in fossils (Fig. 8A). The observed elemental differences between fossils and matrix are reinforced by both μ -XRF and EDS elemental mapping analyses. Elemental maps suggested elevated concentrations of C and Ca, and reduced O, Si, Al, and K concentrations in fossils relative to the matrix (Figs. 5J–U, 6J–P, 9, 10).

The distribution of Fe is non-uniform in different fossils specimens (Figs. 5J–U, 6Q, 10), and to a large extent is closely related to the distribution of framboidal structures revealed in petrographic work (Fig. 4H–O). EDS point analyses on the framboidal structures showed the co-occurrence of Fe, Al, K, and Si (Fig. 4R), suggesting that these structures represent Fe rich clay minerals. These Fe rich clays are rarer in un-weathered material. Other framboidal structures (Fig. 4P–Q, 6H, 7F, 7J–L) with octahedral morphologies, which are present in specimens LTL L0529, LTL C0586 and LTL T1586, have an Fe-oxide composition and may be pyrite pseudomorphs (Fig. 4S; Huang et al., 2019).

Barium was also occasionally detected but only in fossil specimen LTL 0529 where it forms spherical or tabular minerals filling voids (Fig. 6C–G). When occurring, Ba is always present in coincidence with S and O (Fig. 6J–W), suggesting these minerals are barite.

4.4. X-ray diffraction of fossils and their surrounding matrix

XRD documented fossil and matrix mineralogy to understand the origin of elemental differences between fossils and the surrounding matrix seen in EDS and μ -XRF. XRD showed that the 10 fossil specimens analyzed, and their surrounding matrices, are predominantly composed of quartz, K-feldspar, and muscovite (Fig. 8B). In addition, a few other minerals: siderite, anhydrite, cryptohalite, and a few barites are present in fossils and matrix, accounting for only a small fraction of their total compositions (commonly less than <10%). The clay mineral kaolinite was only detected in fossil specimen LTL T1562 and its matrix. Illite/smectite was recorded in fossil specimen LTL L1550. Hence, the clay subtotal (defined here as sum of muscovite, illite/smectite, and kaolinite) depends to a large extent on the content of muscovite (Fig. 8B). In general, the selected-area XRD results were consistent with observations from microscopy, EDS and μ -XRF, and although sample sizes were small, no differences in mineral composition between fossils and the matrix were documented (Fig. 8B).

The host of the Ca enrichments in fossils remains unknown. XRD indicated the element could be hosted in montmorillonite products, such as illite/muscovite (see Broce and Schiffbauer 2017). Alternatively, if Ca is hosted in carbonate minerals, these must make up a small proportion of the overall volume of material analyzed to have escaped detection by XRD (no carbonates were detected although it should be noted that the X-ray beam will penetrate matrix material through the thin fossil compressions diluting any fossil signal).

Despite petrographic and EDS data suggesting Fe rich clay minerals are associated with the fossils, no specific Fe rich clays (e.g., berthierine/chamosite) were detected in XRD. Fe, however, might be hosted within illite/muscovite, which were recorded, and these minerals may in part reflect a diagenetic transformation of an earlier Fe-rich precursor (e.g., Powell, 2003).

4.5. Raman spectral characteristics of the carbonaceous patches in fossils

Raman revealed that the thermal maturity of fossil organic carbon is low. As disordered carbonaceous matter (CM) is graphitized with the enhancement of

metamorphism, the width and intensity of the disordered (D) band decreases and may even disappear, while the graphitic (G) band is narrowed but enhanced. Hence, the maturity of CM can be assessed based on parameters of these two bands, such as the ratio of their intensities (defined as I-1345/1600). All Raman spectra collected from 16 fossil specimens showed two prominent bands at $\sim 1340\text{ cm}^{-1}$ and $\sim 1600\text{ cm}^{-1}$ representing the D and G bands, respectively (Fig. 11). The intense D-band, represented by values of I-1344/1600 ranging from 0.64 to 0.95, indicated fossils were unlikely to have experienced temperatures over $300\text{ }^{\circ}\text{C}$ (Kouketsu et al., 2014). In fact, the peak metamorphic temperature reconstructed by the deconvolution of the D and G bands using Kouketsu et al.'s (2014) method, falls in the range of $190\text{ }^{\circ}\text{C}$ to $250\text{ }^{\circ}\text{C}$. No other mineral phases were identified in association with the carbonaceous patches using Raman spectroscopy.

5. Discussion

5.1. Paleoenvironment analysis: Burial of the Longfengshan biota

The Longfengshan biota has long been thought to have inhabited a restricted tidal environment or a quiet and deeper environment within the euphotic zone, based on the assumed photosynthetic nature of many of the fossil organisms (Du and Tian, 1985, 1986; Du et al., 2009; Liu, 2018; Wang et al., 2021). However, petrographic observations of the fossil-bearing interval have been lacking. The detailed petrographic analysis conducted here sheds light on the habitat of the biota's benthic macroalgae, such as *Longfengshania*.

Dark-light laminae couplets in shales have been interpreted as reflecting growth of benthic microbial mats (dark layers) that were interrupted by high-energy currents (storms or floods) depositing the light layers (Fig. 3A–C; Schieber et al., 2007). This interpretation can be applied to the dark-light laminae couplets present in the fossil horizon of the Luotuoling Formation.

The dark laminae within the fossil horizon suggest that the muddy sea-bed

330 encrusted by sticky microbial mats (Fig. 4A–F) may have provided a cohesive surface
331 for the attachment of the coeval benthic macroalgae such as *Longfengshania* (Cai et al.,
332 2011; Aubineau et al., 2018). It is notable that for macroalgae taking root to anchor on
333 a substratum is equally important as growing upwards in the quest to secure sunlight
334 and nutrients on such a soft and muddy seafloor. In modern marine environments,
335 aquatic plants are often benthic rather than planktonic, attaching themselves to the
336 seafloor and growing upwards at shallow depths. This mode of life ensures that light is
337 consistently accessible for photosynthesis and avoids the problem of being carried by
338 currents to depths where light is insufficient (Kirk, 2011; Hurd et al., 2014). In addition,
339 the movement of water currents caused by tides and wind cycles in these environments
340 enables the algae to utilize nutrients in larger volumes than their neighbors (Kirk, 2011;
341 Hurd et al., 2014).

342 The sticky microbial mats of the dark laminae might also have facilitated relatively
343 oxygen-rich water conditions immediately above the sediment-water interface,
344 promoting the proliferation of benthic macroalgae (Gingras et al., 2011; Lan and Chen,
345 2012; Wang et al., 2021; Chen et al., 2022). Recent Fe speciation data collected from
346 the Luotuoling Formation support this notion, documenting benthic oxygen oases
347 within a ferruginous water-column (Wang et al., 2021). Diffusion-limited conditions,
348 however, may have developed within the sediment due to the sealing effect of microbial
349 mats and our documentation of Fe rich clay minerals is consistent with oxygen-depleted
350 but Fe-replete pore waters (Zatoń et al., 2014; Kloss et al., 2015).

351 The light laminae suggest that water disturbances may have caused the benthic
352 macroalgae, such as *Longfengshania*, to be felled and fall down on the sediments, an
353 inference supported by two observations. First, fragmentary fossil specimens make up
354 the vast majority of our collection, and no traces of holdfast structures are found in our
355 fossils. Second, although most laminae are horizontal and continuous, sedimentary
356 microstructures indicative of sedimentary disturbances such as microscours, erosional
357 surfaces, flakes of fine clay minerals or mat debris, and small-scale cross-stratifications
358 also develop within the laminated mudstone. Of these, flakes of fine clay minerals or
359 mat debris may represent the sedimentation of lag deposits after higher-energy events

(Lan and Chen, 2012; Tu et al., 2016; Xu et al., 2017; Feng et al., 2019; Luo et al., 2019), whereas microsurrows and erosional surfaces may indicate shear and erosion. Recently, taphonomic experiments revealed that non-mineralized organisms such as polychaetes can be transported without major damage (Bath-Enright et al., 2017). With this in mind, transportation or reworking may have been involved in the preservation of the Longfengshan biota (Diniz et al., 2021).

Combined, the fossil-bearing strata were likely deposited in the subtidal zone, below storm wave base, but within the euphotic zone, and were occasionally disturbed by currents or distal storms.

5.2. Formation of calcium enrichments on fossils

Longfengshan fossils display pronounced calcium enrichments compared to their surrounding matrix (Figs. 9, 10). A comparable calcium enrichment in soft tissue fossils has been documented in some Cambrian carbonaceous compressions which share a BST preservation style (Broce and Schiffbauer, 2017; Anderson et al., 2021). Both Fe speciation data (Wang et al., 2021) from the Luotuoling Formation and this study's documentation of Fe in the fossil horizon suggest that Fe was readily available in the depositional system. One way to enrich fossils in calcium is through calcium carbonate formation as a result of the degradation of the macroalgae via microbial iron reduction. This process can increase alkalinity by producing bicarbonate ions, which may raise the calcium carbonate saturation state in the vicinity of decaying organic matter (Allison, 2001; Gallagher et al., 2012; Knoll et al., 2013). In such conditions, calcium carbonate can nucleate on the reactive organic remains. The calcium enrichments on the macroalgae fossils may suggest that microbial iron reduction played a significant role in their post-mortem degradation. As an alternative, Anderson et al (2021) proposed that carbonate precipitation may be encouraged on organic carcasses in sulfate depleted settings due to the initiation of methanogenesis and the anaerobic oxidation of methane. The latter also facilitates the delivery of significant amounts of alkalinity and dissolved inorganic carbon for carbonate precipitation (Compton, 1988; Knittel and Boetius,

2009). In the Luotuoling Formation, sulfate may have been limited consistent with this second hypothesis (Wang et al., 2021).

XRD data from this study, however, found no evidence for calcium carbonate in association with the Longfengshan fossils. This indicates that Ca may not be hosted in a carbonate but rather in a diagenetic product of montmorillonite like illite/muscovite (Mapstone and McIlroy, 2006). Broce and Shiffbauer (2017) argued that calcium in vermiform (worm-like) fossils could be hosted by either calcium carbonate or, interestingly, by calcium-bearing clay minerals like montmorillonite. Montmorillonite is ideally suited to adsorption to organic matter due to its large reactive surface (Kennedy et al., 2002) and may have promoted soft-tissue preservation (Butterfield, 1990).

5.3. Taphonomy of the Longfengshan biota and a possible role for iron

The elemental and mineralogical data we have presented here provide insights into the geochemical conditions that facilitated the preservation of the Longfengshan biota. It is likely that degradation upon death of the macroalgae was initially undertaken by aerobic respiration, however, as a large amount of oxygen was consumed, an anoxic microenvironment may have formed around the decaying organism (Allison, 1988, 2001). Further decay would then proceed through anaerobic microbial degradation such as sulfate reduction. However, evidence suggests that microbial sulfate reduction had a limited role to play in the degradation of the Longfengshan algae. Wang et al. (2021) argued that, during deposition of the Luotuoling Formation, the water column (and thus pore waters) contained little sulfate but was instead Fe-replete. In these Fe-replete pore waters of the Luotuoling sediments, Fe^{2+} ions would be available to form pyrite if sulfide was also present (Canfield, 1989). However, our petrographic and SEM analyses revealed that both fossils and their surrounding matrix contain only minor amounts of pyrite. The fossil-bearing interval therefore likely had relatively low sulfide-generating potential (Sperling et al., 2018), implying the inhibition of sulfate-reducing bacteria or limited sulfate availability (Petrovich, 2001; Gaines et al., 2012; Wacey et al., 2014;

Guan et al., 2017; Anderson et al., 2021). When the ferruginous condition of the porewaters was disrupted, dissolution of any rare pyrite and the resulting dissolved sulfate ions, could prompt local precipitation of barite (Hanor, 2000; Broce and Schiffbauer, 2017). This could account for the barite in or immediately around some cavities which are presumed to result from dissolution of pyrite (Fig. 6C–G).

Instead of forming pyrite in abundance, the Fe^{2+} ions in the Fe-replete pore waters, or Fe^{2+} ions released through the oxidation of carbonaceous matter by potential iron reducing bacteria, may have adsorbed onto carbonaceous matter, helping to inhibit subsequent degradation (Petrovich, 2001). In our samples, both fossils and the matrix possess relatively high Fe concentrations and we have documented Fe rich clay minerals in association with fossils.

The role of clay minerals and specifically Fe-rich clays has been noted for other carbonaceous compression fossils, including those in deposits with BST preservation. Certain clay minerals such as Fe-rich chamosite/berthierine have been argued to be critical to fossil soft-tissue preservation as carbonaceous compressions either by facilitating the polymerization of organic remains or by their toxicity to heterotrophic decay bacteria (Petrovich, 2001; McMahon et al., 2016; Anderson et al., 2018; Saleh et al., 2019; Anderson et al., 2021). The timing of the origin of these minerals is a matter of debate, with the significant age of these deposits and varying diagenetic/metamorphic histories often partially obscuring early diagenetic chemistry (Orr et al., 1998; Butterfield et al., 2007; Page et al., 2008; Anderson et al., 2021; Becker-Kerber et al., 2022; Nielson et al., 2022). In some deposits (e.g., the Cambrian Burgess Shale Formation), the minerals are demonstrably early and so likely played a role in the exceptional preservation of fossil soft tissues (Anderson et al., 2021), while in others (e.g., Ediacaran Tamengo Formation) evidence suggests that they formed significantly after soft tissues were preserved, consequently playing no role in the initial conservation of soft tissues (Becker-Kerber et al., 2022).

Caution should be taken over the role of Fe-rich clays in the preservation of the Longfengshan biota as the timing of their formation is unresolved. Evidence that spheroidal agglomerations of Fe-clays penetrate carbonaceous material (Figs. 5F–I, 7C,

7I, 7N–R) may argue for an early origin. However, the observation that they are more common in weathered samples versus un-weathered may indicate they formed at a later stage.

6. Conclusion

The depositional environment of the fossil-bearing interval and the post-mortem degradation and preservation of the Longfengshan macroalgal fossils were inferred based on a combination of petrographic, geochemical, and mineralogical analyses. Petrography revealed the existence of microbial mats in the fossil-bearing shale, which may have been beneficial to the proliferation of macroalgae in that setting. However, it also provided evidence of episodic event deposits that entombed and preserved the macroalgae. Geochemical and mineralogical analyses showed that they were eventually preserved in anaerobic microenvironments, which, together with the Fe-replete but sulfate-depleted porewater conditions, inhibited further decay and facilitated their preservation of the carbonaceous remains.

Acknowledgements

This study was supported by a NSFC grant (41821001), a National Key R & D Program of China grant (2017YFC0603103), the 111 Program of China (BP0820004), and All Souls College (University of Oxford). We thank Katherine Clayton for assistance with X-ray diffraction at the University of Oxford and Nicholas Tosca (University of Cambridge) for valuable discussion. We thank Liqing Sun and Yuanyuan Wu for assistance with micro X-ray fluorescence spectroscopy at Buoyue Instruments Co. Ltd in Shanghai, China. Qing Tang, two anonymous reviewer, and guest editor Xingliang Zhang are acknowledged for their constructive comments, which have greatly improved the quality of the paper.

References

480

481 Allison, P.A., 1988. The role of anoxia in the decay and mineralization of proteinaceous
482 macro-fossils. *Paleobiology* 14, 139–154.

483 Allison, P.A., 2001. Fossilization processes. In: Briggs, D.E.G., Crowther, P.R. (Eds.),
484 *Palaeobiology II*. Blackwell Science, Oxford, pp. 270–273.

485 Anderson, E.P., Schiffbauer, J.D., Xiao, S., 2011. Taphonomic study of Ediacaran
486 organic-walled fossils confirms the importance of clay minerals and pyrite in
487 Burgess Shale–type preservation. *Geology* 39, 643–646.

488 Anderson, R.P., Tosca, N.J., Gaines, R.R., Koch, N.M., Briggs, D.E.G., 2018. A
489 mineralogical signature for Burgess Shale–type fossilization. *Geology* 46, 347–
490 350.

491 Anderson, R.P., Tosca, N.J., Cinque, G., Frogley, M.D., Lekkas, I., Akey, A., Hughes,
492 G.M., Bergmann, K.D., Knoll, A.H., Briggs, D.E.G., 2020. Aluminosilicate haloes
493 preserve complex life approximately 800 million years ago. *Interface Focus* 10,
494 20200011.

495 Anderson, R.P., Tosca, N.J., Saupe, E.E., Wade, J., Briggs, D.E.G., 2021. Early
496 formation and taphonomic significance of kaolinite associated with Burgess Shale
497 fossils. *Geology* 49, 355–359.

498 Aubineau, J., El Albani, A., Chi Fru, E., Gingras, M., Batonneau, Y., Buatois, L.A.,
499 Geffroy, C., Labanowski, J., Laforest, C., Lemée, L.J.G., 2018. Unusual microbial
500 mat-related structural diversity 2.1 billion years ago and implications for the
501 Francevillian biota. *Geobiology* 16, 476–497.

502 Bath-Enright, O.G., Minter, N.J., Sumner, E.J., 2017. Palaeoecological implications of
503 the preservation potential of soft-bodied organisms in sediment-density flows:
504 testing turbulent waters. *R. Soc. Open Sci.* 4, 170212.

505 Becker-Kerber, B., Elmola, A.A., Zhuravlev, A., Gaucher, C., Simões, M.G., Prado,
506 G.M.E.M., Vintaned, J.A.G., Fontaine, C., Lino, L.M., Sanchez, D.F., Galante, D.,
507 Paim, P.S.G., Callefo, F., Kerber, G., Meunier, A., Albani, A.E., 2022. Clay
508 templates in Ediacaran vendotaeniaceans: Implications for the taphonomy of
509 carbonaceous fossils. *Geol. Soc. Am. Bull.* 134, 1334–1346.

- Broce, J.S., Schiffbauer, J.D., 2017. Taphonomic analysis of Cambrian vermiform fossils of Utah and Nevada, and implications for the chemistry of Burgess Shale-type preservation. *Palaios* 32, 600–619.
- Butterfield, N.J., 1990. Organic preservation of non-mineralizing organisms and the taphonomy of the Burgess Shale. *Paleobiology* 16, 272–286.
- Butterfield, N.J., 1995. Secular distribution of Burgess-Shale-type preservation. *Lethaia* 28, 1–13.
- Butterfield, N.J., Balthasar, U., Wilson, L.A., 2007. Fossil diagenesis in the Burgess Shale. *Palaeontology* 50, 537–543.
- Bykova, N., LoDuca, S.T., Ye, Q., Marusin, V., Grazhdankin, D., Xiao, S., 2020. Seaweeds through time: Morphological and ecological analysis of Proterozoic and early Paleozoic benthic macroalgae. *Precambr. Res.* 350, 105875.
- Cai, Y., Schiffbauer, J.D., Hua, H., Xiao, S., 2011. Morphology and paleoecology of the late Ediacaran tubular fossil *Conotubus hemiannulatus* from the Gaojiashan Lagerstätte of southern Shaanxi Province, South China. *Precambr. Res.* 191, 46–57.
- Cai, Y., Schiffbauer, J.D., Hua, H., Xiao, S., 2012. Preservational modes in the Ediacaran Gaojiashan Lagerstätte: Pyritization, aluminosilicification, and carbonaceous compression. *Palaeogeogr. Palaeoclimatol. Palaeoecol.* 326–328, 109–117.
- Canfield, D.E., 1989. Reactive iron in marine sediments. *Geochim. Cosmochim. Acta* 53, 619–632.
- Chen, Z.Q., Wang, Y., Kershaw, S., Luo, M., Yang, H., Zhao, L., Feng, Y., Chen, J., Yang, L., Zhang, L., 2014. Early Triassic stromatolites in a siliciclastic nearshore setting in northern Perth Basin, Western Australia: Geobiologic features and implications for post-extinction microbial proliferation. *Glob. Planet. Chang.* 121, 89–100.
- Chen, Z.Q., Fang, Y.H., Wignall, P.B., Guo, Z., Wu, S.Q., Liu, Z.L., Wang, R.Q., Huang, Y.G., Feng, X.Q., 2022. Microbial blooms triggered pyrite framboid enrichment and oxygen depletion in carbonate platforms immediately after the latest Permian

540 extinction. *Geophys. Res. Lett.* 49, e2021GL096998.

541 Cohen, P.A., Macdonald, F.A., 2015. The Proterozoic record of eukaryotes.
542 *Paleobiology* 41, 610–632.

543 Cohen, P.A., Kodner, R.B., 2022. The earliest history of eukaryotic life: Uncovering an
544 evolutionary story through the integration of biological and geological data.
545 *Trends Ecol. Evol.* 37, 246–256.

546 Compton, J.S., 1988. Degree of supersaturation and precipitation of organogenic
547 dolomite. *Geology* 16, 318–321.

548 Diniz, C.Q.C., Leme, J.d.M., Boggiani, P.C., 2021. New Species of Macroalgae from
549 Tamengo Formation, Ediacaran, Brazil. *Front. Earth Sci.* 9, 748876.

550 Du, R., Tian, L., 1985. Algal macrofossils from the Qingbaikou system in the Yanshan
551 range of North China. *Precambr. Res.* 29, 5–14.

552 Du, R., Tian, L., 1986. The macroalgal fossils of the Qingbaikou period in Yanshan
553 range. Hebei Science and Technology Press, Shijiazhuang (in Chinese with
554 English Abstract).

555 Du, R., Tian, L., Hu, H., Sun, L., Chen, J., 2009. The Neoproterozoic Qingbaikou period
556 Longfengshan biota. Chinese Science Press, Beijing (in Chinese with English
557 Abstract).

558 Fang, Y., Chen, Z.Q., Kershaw, S., Yang, H., Luo, M., 2017. Permian-Triassic boundary
559 microbialites at Zuodeng Section, Guangxi Province, South China: Geobiology
560 and palaeoceanographic implications. *Glob. Planet. Chang.* 152, 115–128.

561 Feng, X.Q., Chen, Z.Q., Bottjer, D.J., Wu, S.Q., Zhao, L.S., Xu, Y.L., Shi, G.R., Huang,
562 Y.G., Fang, Y.H., Tu, C.Y., 2019. Unusual shallow marine matground-adapted
563 benthic biofacies from the Lower Triassic of the northern Paleotethys:
564 Implications for biotic recovery following the end-Permian mass extinction. *Earth-*
565 *Sci. Rev.* 189, 194-219.

566 Forchielli, A., Steiner, M., Kasbohm, J., Hu, S., Keupp, H., 2014. Taphonomic traits of
567 clay-hosted early Cambrian Burgess Shale-type fossil Lagerstätten in South China.
568 *Palaeogeogr. Palaeoclimatol. Palaeoecol.* 398, 59–85.

569 Gabbott, S.E., Hou, X., Norry, M.J., Siveter, D.J., 2004. Preservation of Early Cambrian

570 animals of the Chengjiang biota. *Geology* 32, 901–904

571 Gaines, R.R., Briggs, D.E.G., Zhao, Y., 2008. Cambrian Burgess Shale-type deposits
572 share a common mode of fossilization. *Geology* 36, 755–758.

573 Gaines, R.R., Hammarlund, E.U., Hou, X., Qi, C., Gabbott, S.E., Zhao, Y., Peng, J.,
574 Canfield, D.E., 2012. Mechanism for Burgess Shale-type preservation. *Proc. Natl.*
575 *Acad. Sci. U.S.A.* 109, 5180–5184.

576 Gaines, R.R., 2014. Burgess Shale-type preservation and its distribution in space and
577 time. *Paleontol. Soc. Pap.* 20, 123–146.

578 Gallagher, K.L., Kading, T.J., Braissant, O., Dupraz, C., Visscher, P.T., 2012. Inside the
579 alkalinity engine: The role of electron donors in the organomineralization potential
580 of sulfate-reducing bacteria. *Geobiology* 10, 518–530.

581 Gingras, M., Hagadorn, J.W., Seilacher, A., Lalonde, S.V., Pecoits, E., Petrash, D.,
582 Konhauser, K.O., 2011. Possible evolution of mobile animals in association with
583 microbial mats. *Nat. Geosci.* 4, 372–375.

584 Guan, C., Wang, W., Zhou, C., Muscente, A.D., Wan, B., Chen, X., Yuan, X., Chen, Z.,
585 Ouyang, Q., 2017. Controls on fossil pyritization: Redox conditions, sedimentary
586 organic matter content, and *Chuaria* preservation in the Ediacaran Lantian Biota.
587 *Palaeogeogr. Palaeoclimatol. Palaeoecol.* 474, 26–35.

588 Halverson, G., Porter, S., Shields, G., 2020. The Tonian and Cryogenian Periods. In:
589 Gradstein, F.M., Ogg, J.G., Schmitz, M.D., Ogg, G.M. (eds), *Geologic Time Scale*
590 2020. Volume 1, pp. 495–519, Elsevier, Amsterdam, Netherlands.

591 Hanor, J.S., 2000. Barite–celestine geochemistry and environments of formation. *Rev.*
592 *Mineral. Geochem.* 40, 193–275.

593 Hofmann, H.J., 1985. The Mid-Proterozoic Little Dal macrobiota, Mackenzie
594 Mountains, North-west Canada. *Palaeontology* 28, 331–354.

595 Huang, Y.G., Chen, Z.Q., Algeo, T.J., Zhao, L.S., Baud, A., Bhat, G.M., Zhang, L., Guo,
596 Z., 2019. Two-stage marine anoxia and biotic response during the Permian-
597 Triassic transition in Kashmir, northern India: pyrite framboid evidence. *Glob.*
598 *Plane. Chang.* 172, 124–139.

599 Hurd, C.L., Harrison, P.J., Bischof, K., Lobban, C.S., 2014. Seaweed ecology and

physiology. University Printing House, Cambridge, 551 pp.

Jin, Z.K., Zhu, X.E., Wang, J.Y., Wang, X.Y., Ren, Y.L., Wang, L., Guo, Q.H., Li Y., Shi, S.T., Li, S., Yuan, K., Li, R., Yan, W., 2020. Field guide of stratigraphy and sedimentary facies of the Proterozoic in Jizhou District, Tianjin. China University of Petroleum, Beijing, 272 pp.

Jing, Y., Chen, Z.Q., Tu, C., 2022. A late Paleoproterozoic microfossil community from siliceous granules, Dahongyu Formation, North China. *Precambr. Res.* 377, 106723.

Kennedy, M.J., Reveal, D.R., Hill, R.J., 2002. Mineral surface control of organic carbon in black shale. *Science* 295, 657–660.

Kirk, T.O., 2011. Light and photosynthesis in aquatic ecosystems. Cambridge University Press, New York, 649 pp.

Kloss, T.J., Dornbos, S.Q., Chen, J., McHenry, L.J., Marengo, P.J., 2015. High-resolution geochemical evidence for oxic bottom waters in three Cambrian Burgess Shale-type deposits. *Palaeogeogr. Palaeoclimatol. Palaeoecol.* 440, 90–95.

Knittel, K., Boetius, A., 2009. Anaerobic oxidation of methane: Progress with an unknown process. *Annu. Rev. Microbiol.* 63, 311–334.

Knoll, A.H., Wörndle, S., Kah, L., 2013. Covariance of microfossil assemblages and microbialite textures across an upper Mesoproterozoic carbonate platform. *Palaios* 28, 453–470.

Kouketsu, Y., Mizukami, T., Mori, H., Endo, S., Aoya, M., Hara, H., Nakamura, D., Wallis, S., 2014. A new approach to develop the Raman carbonaceous material geothermometer for low-grade metamorphism using peak width. *Isl. Arc* 23, 33–50.

Lan, Z.W., Chen, Z.Q., 2012. Exceptionally preserved microbially induced sedimentary structures from the Ediacaran post-glacial successions in the Kimberley region, northwestern Australia. *Precambr. Res.* 200, 1–25.

Liu, A., 2018. The characteristics and geological significance of Longfengshan macroalgal biota in Tonian, Neoproterozoic, Hebei Hualai. PhD Thesis, China

University of Geosciences (Wuhan), Wuhan (in Chinese with English abstract).

Luo, M., Chen, Z.Q., Shi, G.R., Feng, X.Q., Yang, H., Fang, Y.H., Li, Y., 2019. Microbially induced sedimentary structures (MISSs) from the Lower Triassic Kockatea Formation, northern Perth Basin, Western Australia: Palaeoenvironmental implications. *Palaeogeogr. Palaeoclimatol. Palaeoecol.* 519, 236–247.

Lyons, T.W., Reinhard, C.T., Planavsky, N.J., 2014. The rise of oxygen in Earth's early ocean and atmosphere. *Nature* 506, 307–315.

Maloney, K.M., Schiffbauer, J.D., Halverson, G.P., Xiao, S., Laflamme, M., 2022. Preservation of early Tonian macroalgal fossils from the Dolores Creek Formation, Yukon. *Sci. Rep.* 12, 6222.

Mapstone, N.B., McIlroy, D., 2006. Ediacaran fossil preservation: Taphonomy and diagenesis of a discoid biota from the Amadeus Basin, central Australia. *Precamb. Res.* 149, 126–148.

McMahon, S., Anderson, R.P., Saupe, E.E., Briggs, D.E.G., 2016. Experimental evidence that clay inhibits bacterial decomposers: Implications for preservation of organic fossils. *Geology* 44, 867–870.

Meyer, M., Schiffbauer, J.D., Xiao, S., Cai, Y., Hua, H., 2012. Taphonomy of the upper Ediacaran enigmatic ribbonlike fossil *Shaanxilithes*. *Palaaios* 27, 354–372.

Nielsen, M.L., Lee, M., Ng, H.C., Rushton, J.C., Hendry, K.R., Kihm, J.-H., Nielsen, A.T., Park, T.-Y.S., Vinther, J., Wilby, P.R., 2022. Metamorphism obscures primary taphonomic pathways in the early Cambrian Sirius Passet Lagerstätte, North Greenland. *Geology* 50, 4–9.

Orr, P.J., Briggs, D.E.G., Kearns, S.L., 1998. Cambrian Burgess Shale animals replicated in clay minerals. *Science* 281, 1173–1175.

Page, A., Gabbott, S.E., Wilby, P.R., Zalasiewicz, J.A., 2008. Ubiquitous Burgess Shale-style “clay templates” in low-grade metamorphic mudrocks. *Geology* 36, 855–858.

Petrovich, R., 2001. Mechanisms of fossilization of the soft-bodied and lightly armored faunas of the Burgess Shale and of some other classical localities. *Am. J. Sci.* 301,

660 683–726.

661 Powell, W., 2003. Greenschist-facies metamorphism of the Burgess Shale and its
662 implications for models of fossil formation and preservation. *Can. J. Earth Sci.*
663 40,13–25.

664 Saleh, F., Pittet, B., Perrillat, J-P., Lefebvre, B., 2019. Orbital control on exceptional
665 fossil preservation. *Geology* 47, 103–106.

666 Schieber, J., Bose, P.K., Eriksson, P.G., Banerjee, S., Sarkar, S., Altermann, W.,
667 Catuneanu, O., 2007. *Atlas of Microbial Mat Features Preserved within the*
668 *Siliciclastic Rock Record*. Elsevier, Amsterdam, 311 pp.

669 Sperling, E.A., Balthasar, U., Skovsted, C.B., 2018. On the edge of exceptional
670 preservation: insights into the role of redox state in Burgess Shale-type
671 taphonomic windows from the Mural Formation, Alberta, Canada. *Emerg. Top.*
672 *Life Sci.* 2, 311–323.

673 Tang, Q., Pang, K., Yuan, X., Xiao, S., 2020. A one-billion-year-old multicellular
674 chlorophyte. *Nat. Ecol. Evol.* 4, 543–549.

675 Tu, C., Chen, Z-Q., Retallack, G.J., Huang, Y., Fang, Y., 2016. Proliferation of MISS-
676 related microbial mats following the end-Permian mass extinction in terrestrial
677 ecosystems: Evidence from the Lower Triassic of the Yiyang area, Henan Province,
678 North China. *Sediment. Geol.* 333, 50–69.

679 Wacey, D., Saunders, M., Roberts, M., Menon, S., Green, L., Kong, C., Culwick, T.,
680 Strother, P., Brasier, M.D., 2014. Enhanced cellular preservation by clay minerals
681 in 1 billion-year-old lakes. *Sci. Rep.* 4, 5841.

682 Wang, H., Liu, A., Li, C., Feng, Q., Tang, S., Cheng, M., Algeo, T.J., 2021. A benthic
683 oxygen oasis in the early Neoproterozoic ocean. *Precambr. Res.* 355, 106085.

684 Wu, S., Chen, Z.Q., Fang, Y., Pei, Y., Yang, H., Ogg, J., 2017. A Permian-Triassic
685 boundary microbialite deposit from the eastern Yangtze Platform (Jiangxi
686 Province, South China): Geobiologic features, ecosystem composition and redox
687 conditions. *Palaeogeogr. Palaeoclimatol. Palaeoecol.* 486, 58–73.

688 Xiao, S., Dong, L., 2006. On the morphological and ecological history of Proterozoic
689 macroalgae. In: Xiao, S., Kaufman, A.J. (Eds.), *Neoproterozoic Geobiology and*

- Paleobiology. Springer, Dordrecht, the Netherlands, pp. 57–90.
- Xiao, S., Tang, Q., 2018. After the boring billion and before the freezing millions: Evolutionary patterns and innovations in the Tonian Period. *Emerg. Top. Life Sci.* 2, 161–171.
- Xu, Y.L., Chen, Z.Q., Feng, X.Q., Wu, S.Q., Shi, G.R., Tu, C.Y., 2017. Proliferation of MISS-related microbial mats following the end-Permian mass extinction in the northern Paleo-Tethys: Evidence from southern Qilianshan region, western China. *Palaeogeogr. Palaeoclimatol. Palaeoecol.* 474, 198–213.
- Yang, H., Chen, Z.Q., Papineau, D., 2022. Cyanobacterial spheroids and other biosignatures from microdigitate stromatolites of Mesoproterozoic Wumishan Formation in Jixian, North China. *Precambr. Res.* 106496.
- Zatoń M., Filipiak, P., Rakociński, M., Krawczyński, W., 2014. Kowala Lagerstätte: Late Devonian arthropods and non-biomineralized algae from Poland. *Lethaia* 47, 352–364.
- Zhu, M., Babcock, L.E., Steiner, M., 2005. Fossilization modes in the Chengjiang Lagerstätte (Cambrian of China): testing the roles of organic preservation and diagenetic alteration in exceptional preservation. *Palaeogeogr. Palaeoclimatol. Palaeoecol.* 220, 31–46.
- Zhu, S.X., Zhu, M.Y., Knoll, A.H., Yin, Z.J., Zhao, F.C., Sun, S.F., Qu, Y.G., Shi, M., Liu, H., 2016. Decimetre-scale multicellular eukaryotes from the 1.56-billion-year-old Gaoyuzhuang Formation in North China. *Nat. Commun.* 7, 11500.

Figure Captions

Fig. 1. (A) Location of the North China craton in China. (B) Map of the North China craton showing the Proterozoic outcrops in grey color. Star indicates the Changlongshan locality. Modified from Zhu et al. (2016). (C) Generalized stratigraphy of the Luotuoling Formation exposed in the Changlongshan locality, Hebei Province, North China. JEY and XML represent Jingeryu and Xiamaling, respectively.

Fig. 2. Field photographs of the Changlongshan locality showing sampling locations and the lithology of the Luotuoling Formation. (A–B) Overviews of the outcrop in the Changlongshan locality, with red dash line in (A) indicating the unconformable contact between the Xiamaling and Luotuoling formations. Red lines in (B) mark the tops of Member I and Member II of the Luotuoling Formation, respectively. (C) Coarse-grained sandstone in the lower part of Member I. Red lines indicate wavy laminations and black lines mark cross-bedding. (D) Herringbone cross-beddings in Member I points to a tidal environment. (E) Lenticular and wavy laminations in Member I indicate a shallow high energy environment. (F) A large sandstone lens in Member I, with red line indicating sharp erosional surfaces. (G) Grey to black laminated shales of Member II that yield fossils. (H) Freshly exposed shale of the fossil-bearing layers. Note the weathered surfaces (arrowheads) yielding a yellowish-reddish color. (I) Multiple fossil specimens preserved on a bedding surface. (J) Two prominent *Longfengshania* specimens on a bedding surface. (K) Fragmentary specimens and organic debris preserved as highly reflective carbonaceous films on bedding surfaces.

Fig. 3. Photographs of selected fossil specimens of the representative taxa in the Longfengshan biota from the Changlongshan locality: *Longfengshania* (A), *Tawuia* (B), and *Chuaria* (C). For all the photographs, single lines represent scale = 5 mm, double lines = 2 mm.

Fig. 4. Sedimentary and diagenetic fabrics of the fossiliferous silty shale (layer 22, lower Member II) in the Changlongshan locality. (A–C) Polished transverse slabs of the fossil-bearing silty shale showing dark-light laminae couplets. Red dashed lines mark erosion surfaces with sand-sized quartz grains immediately above them. Red arrows in (B) denote flakes of carbonaceous debris in finely laminated siltstone. Note the small-scale cross bedding in (C). (D–F) Cross-section photomicrographs of the fossiliferous silty shale showing microbial mats. Red arrows in (E) and (F) indicate tufted microbial mats. (G) Cross-section photomicrograph showing a microscour structure with sand-sized quartz grains at the base of a light lamina. (H, J)

Photomicrographs showing aggregates of Fe rich minerals occurring in the light and dark laminae, respectively. Note the aligned muscovite flakes (red arrows). (I) Close-up of the boxed area in (H) showing Fe rich minerals with framboidal texture. (K, M) SEM images showing aggregated rosettes of platelets enclosed by thick crusts occurring in clay mineral matrix. Where the aggregated minerals are lost, voids are formed (red arrows). (L) Close-up of the boxed area in (K) showing aggregated rosettes of platelets. (N–O) SEM images showing aggregated rosettes of platelets and the thick crusts (red dashed lines) of the same composition. (P–Q) SEM images showing pyrite framboids that have been oxidized. (R) EDS point spectrum of the red dot in (L) indicating its elemental composition. Note that Fe, O, Si, and Al contents are high. (S) EDS point spectrum of the red dot in (Q) indicating its elemental composition. Note that Fe content is much higher than others.

Fig. 5. Photographs, reflected light photomicrographs, SEM images, and EDS elemental maps of specimen LTL L0129-1 and specimen LTL L0129-2. (A–B) Photographs of *Longfengshania* specimen LTL L0129-1 and its counterpart LTL L0129-2. Yellow boxes show the regions examined in (C–I). (C–E) Close-ups of boxed area in (A) showing the brown to black carbonaceous patches. (F) SEM image of the boxed area in (E) showing the carbonaceous patches and the closely associated Fe rich clay minerals. Yellow dashed line corresponds to fossil edge. Arrowheads indicate the void structures. (G–H) SEM images showing the carbonaceous patches and the void structures. Yellow dashed line in (G) corresponds to fossil edge. (I) Close-up of the boxed area in (H) showing a void structure with aggregated rosettes of platelets enclosed by a thick crust. (J–Q) Elemental maps of the same area as in (F) showing the coincidence of C and Ca on the carbonaceous patches. Note that the elemental maps of C and Fe do not share the same distribution, indicating incomplete replacement of the carbonaceous patches by Fe rich clay minerals. (R–U) Elemental maps of the same area as in (G) showing elevated C and Ca abundance on the carbonaceous patches and the incomplete replacement of carbonaceous patches by Fe rich clay minerals.

Fig. 6. Photographs, reflected light photomicrographs, SEM images, and EDS elemental maps of specimen LTL L0529. (A) Photograph of *Longfengshania* specimen LTL L0529. Yellow boxes denote the region examined in (B–J). (B) Reflected light photomicrographs showing the black carbonaceous patches. (C–G) SEM images showing the voids, some filled by spherical or tabular barite minerals. Note the molds of dissolved pyrite crystals with straight facets (red arrows) in (D). (E) Enlarged view of the boxed area in (D). (H) SEM image showing framboids which were partly dissolved, some still retaining their euhedral crust but empty inside (red arrows). (I–J) SEM images showing the carbonaceous patches and the voids which are occasionally filled with barite minerals. (K–R) Elemental maps of the same area as in (J) showing elevated C and Ca abundance on the carbonaceous patches. Note the barite minerals filled in the voids (O, R). (S–W) Elemental maps of the boxed area in (C).

Fig. 7. Photographs and SEM images of *Chuaria* specimen LTL C0586, *Tawuia* specimen LTL T1586, and *Chuaria* specimen LTL C1598. (A) Photograph of unweathered *Chuaria* specimen LTL C0586. (B) SEM image showing the carbonaceous patches and the void structures. (C) SEM image showing carbonaceous patches inlaid with Fe rich minerals. (D) SEM image showing voids with internal morphology like the cavities formed by removal of pyrite framboids due to weathering. (F) SEM image showing now-hollow euhedral pyrite crystals. (G) Photograph of weathered *Tawuia* specimen LTL T1586. (H) SEM image showing carbonaceous patches. (I) SEM image showing Fe rich clay minerals embedded in carbonaceous patches. (J–L) SEM images showing framboids. (M) Photograph of weathered *Chuaria* specimen LTL C1598. (N–O) SEM images showing the carbonaceous patches and the void structures. (P) SEM image showing aggregated rosettes of platelets enclosed by thick crusts. (Q–R) SEM images showing Fe rich clay minerals embedded in carbonaceous patches. (R) Close-up of boxed area in (Q).

Fig. 8. EDS point analyses and selected-area XRD results. (A) Box plot of the EDS point spectra for the eight analyzed specimens. Note the elevated concentrations of C and Ca, and reduced O, Si, Al, and K concentrations in the fossils relative to the matrices. (B) Box plot of the selected-area XRD data showing the mineral compositions of the fossils and their respective matrices.

Fig. 9. Photograph and μ -XRF elemental maps of specimen LTL L0429 showing the prominent enrichment of calcium within fossils relative to the surrounding matrix. (A) Photograph of specimen LTL L0429. (B–F) Elemental maps of the same area as in (A) showing the distribution of elements O, Al, Si, K, and Ca. Brightness of color corresponds to abundance of each element. Scale bar in (A) represents 5 mm and the same for (B–F).

Fig. 10. Photographs and EDS elemental maps of the eight analyzed fossil specimens. All specimens show elevated concentrations of C and Ca, and reduced O, Si, Al, and K concentrations relative to the matrix. Brightness of color corresponds to abundance of each element. Scale bar represents 2 mm in (A–G).

Fig. 11. (A) Reflected light photomicrographs and the confocal laser Raman spectra of the carbonaceous patches of the 16 analyzed fossil specimens. Spectra were probed on the surface of the carbonaceous patches, indicating the carbonaceous nature of fossils. Position of the probed sites are marked by red and blue crosses in reflected light photomicrographs.

Table Captions

Table 1. Summary of EDS point spectral data for eight specimens from the Luotuoling Formation. Data for fossils obtained from carbonaceous patches that are macroalgal remains, and for matrix obtained from surrounding host rock with no carbonaceous

remains. All elemental point data are reported in normalized weight percentage (nwp). Elements are organized from left to right according to their atomic number.

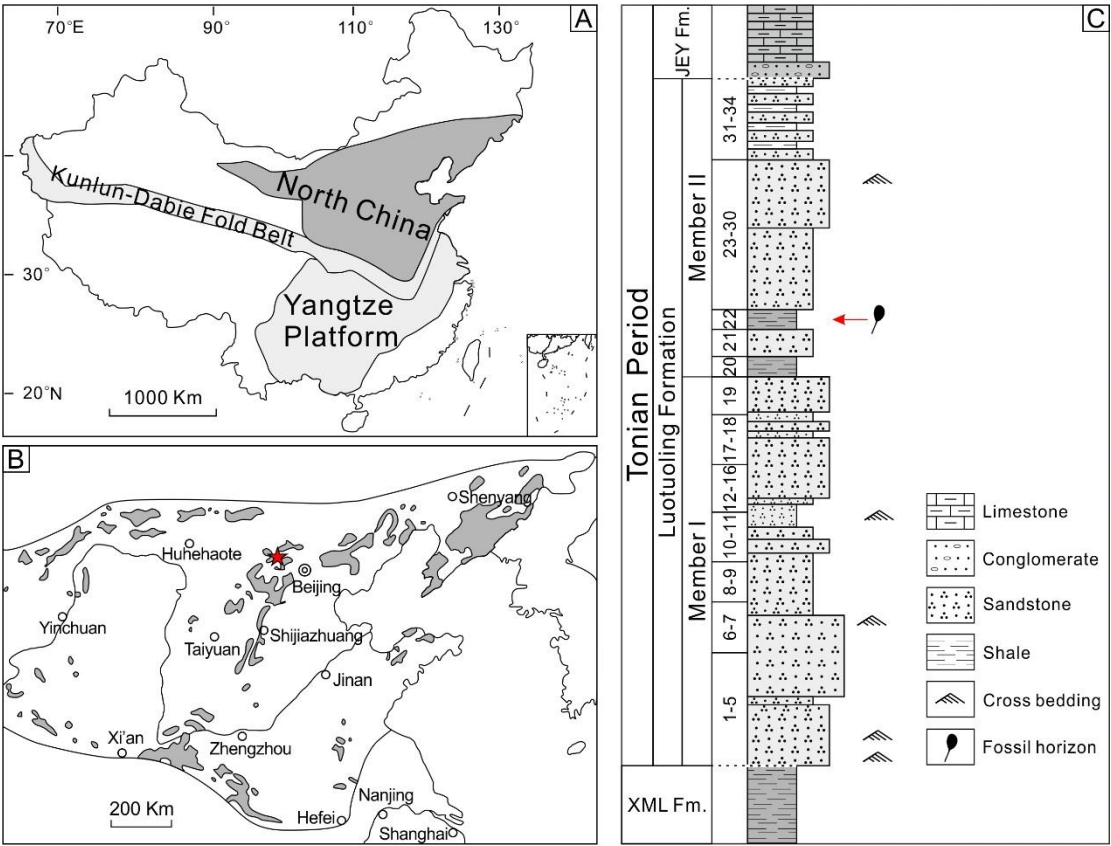


Fig. 1. (A) Location of the North China craton in China. (B) Map of the North China craton showing the Proterozoic outcrops in grey color. Star indicates the Changlongshan locality. Modified from Zhu et al. (2016). (C) Generalized stratigraphy of the Luotuoling Formation exposed in the Changlongshan locality, Hebei Province, North China. JEY and XML represent Jingeryu and Xiamaling, respectively.

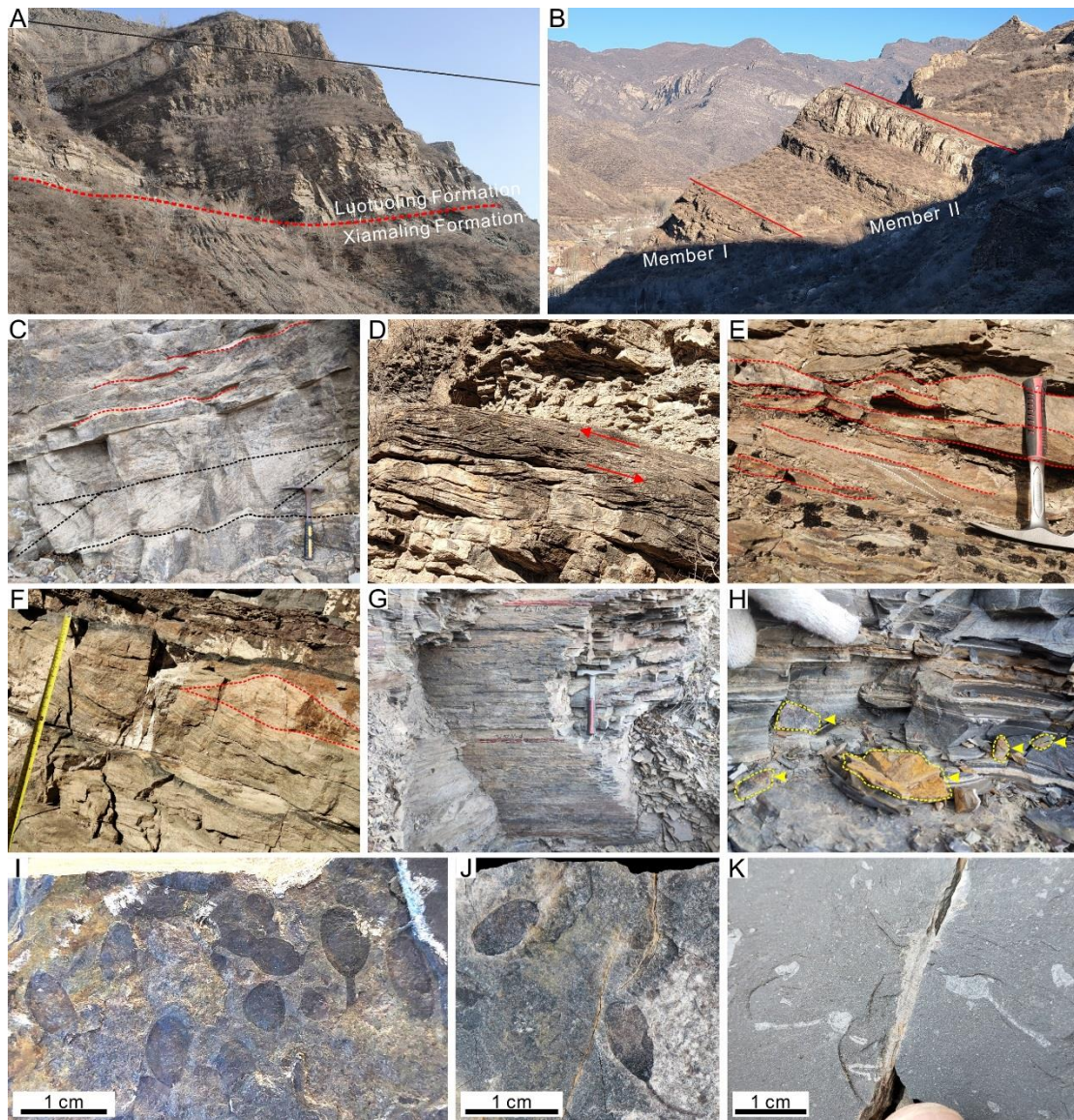


Fig. 2. Field photographs of the Changlongshan locality showing sampling locations and the lithology of the Luotuling Formation. (A–B) Overviews of the outcrop in the Changlongshan locality, with red dash line in (A) indicating the unconformable contact between the Xiamaling and Luotuling formations. Red lines in (B) mark the tops of Member I and Member II of the Luotuling Formation, respectively. (C) Coarse-grained sandstone in the lower part of Member I. Red lines indicate wavy laminations and black lines mark cross-bedding. (D) Herringbone cross-beddings in Member I points to a tidal environment. (E) Lenticular and wavy laminations in Member I indicate a shallow high energy environment. (F) A large sandstone lens in Member I, with red line indicating sharp erosional surfaces. (G) Grey to black laminated shales of Member II that yield fossils. (H) Freshly exposed shale of the fossil-bearing layers. Note the

weathered surfaces (arrowheads) yielding a yellowish-reddish color. (I) Multiple fossil specimens preserved on a bedding surface. (J) Two prominent *Longfengshania* specimens on a bedding surface. (K) Fragmentary specimens and organic debris preserved as highly reflective carbonaceous films on bedding surfaces.

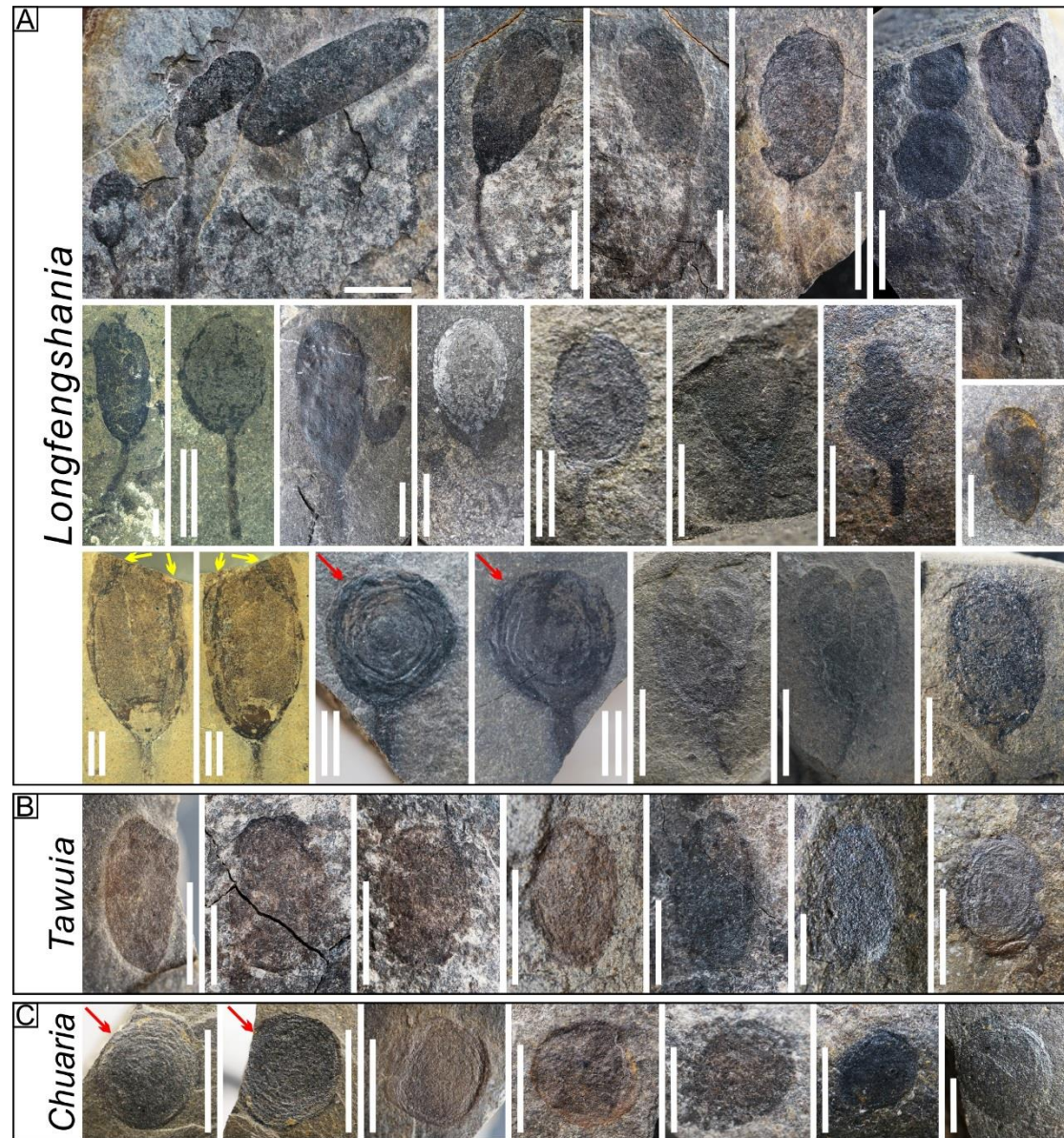


Fig. 3. Photographs of selected fossil specimens of the representative taxa in the Longfengshan biota from the Changlongshan locality: *Longfengshania* (A), *Tawuia* (B), and *Chuarua* (C). For all the photographs, single lines represent scale = 5 mm, double lines = 2 mm.

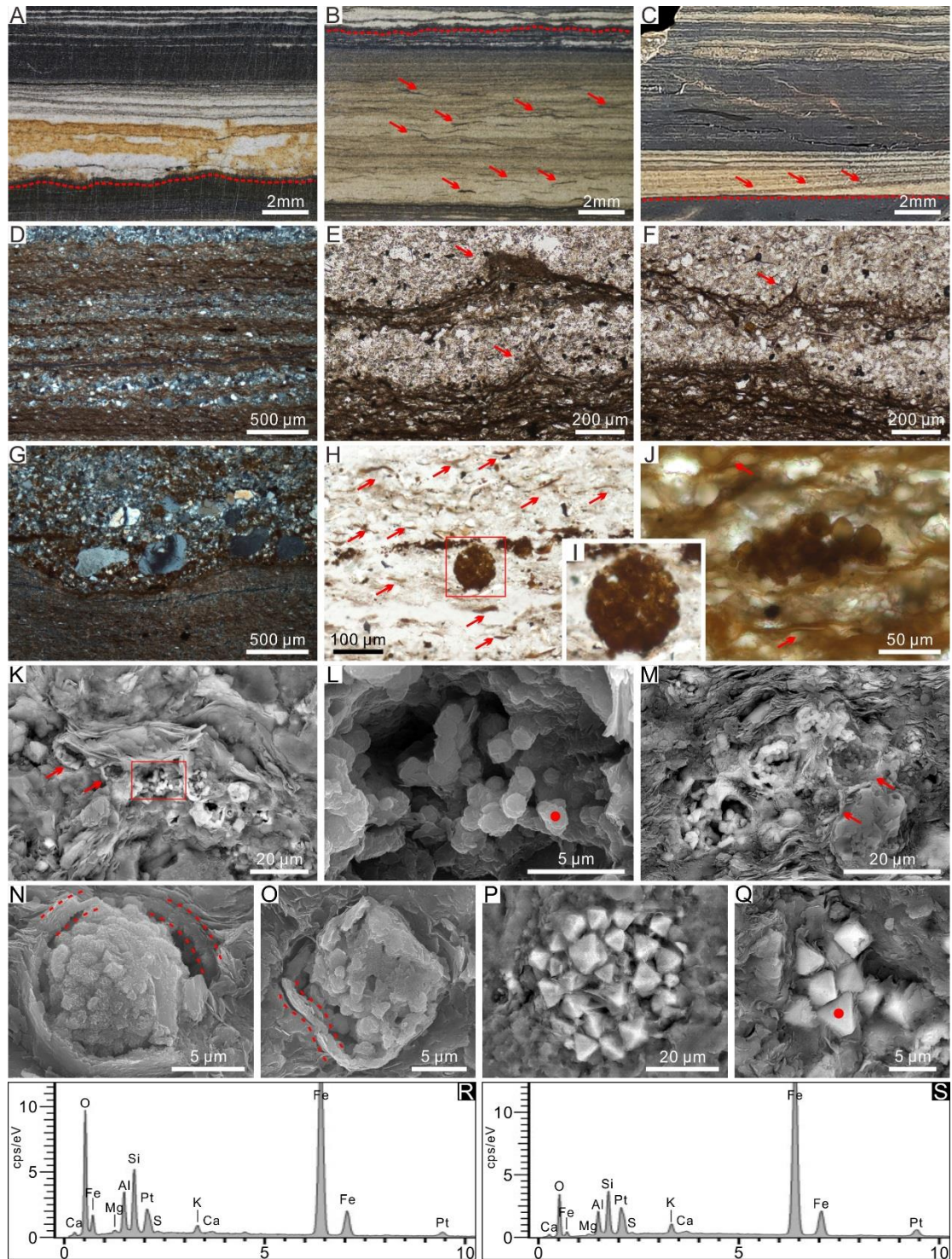


Fig. 4. Sedimentary and diagenetic fabrics of the fossiliferous silty shale (layer 22, lower Member II) in the Changlongshan locality. (A–C) Polished transverse slabs of the fossil-bearing silty shale showing dark-light laminae couplets. Red dashed lines mark erosion surfaces with sand-sized quartz grains immediately above them. Red arrows in (B) denote flakes of carbonaceous debris in finely laminated siltstone. Note the small-scale cross bedding in (C). (D–F) Cross-section photomicrographs of the

fossiliferous silty shale showing microbial mats. Red arrows in (E) and (F) indicate
tufted microbial mats. (G) Cross-section photomicrograph showing a microscour
structure with sand-sized quartz grains at the base of a light lamina. (H, J)
Photomicrographs showing aggregates of Fe rich minerals occurring in the light and
dark laminae, respectively. Note the aligned muscovite flakes (red arrows). (I) Close-
up of the boxed area in (H) showing Fe rich minerals with framboidal texture. (K, M)
SEM images showing aggregated rosettes of platelets enclosed by thick crusts
occurring in clay mineral matrix. Where the aggregated minerals are lost, voids are
formed (red arrows). (L) Close-up of the boxed area in (K) showing aggregated rosettes
of platelets. (N–O) SEM images showing aggregated rosettes of platelets and the thick
crusts (red dashed lines) of the same composition. (P–Q) SEM images showing pyrite
framboids that have been oxidized. (R) EDS point spectrum of the red dot in (L)
indicating its elemental composition. Note that Fe, O, Si, and Al contents are high. (S)
EDS point spectrum of the red dot in (Q) indicating its elemental composition. Note
that Fe content is much higher than others.

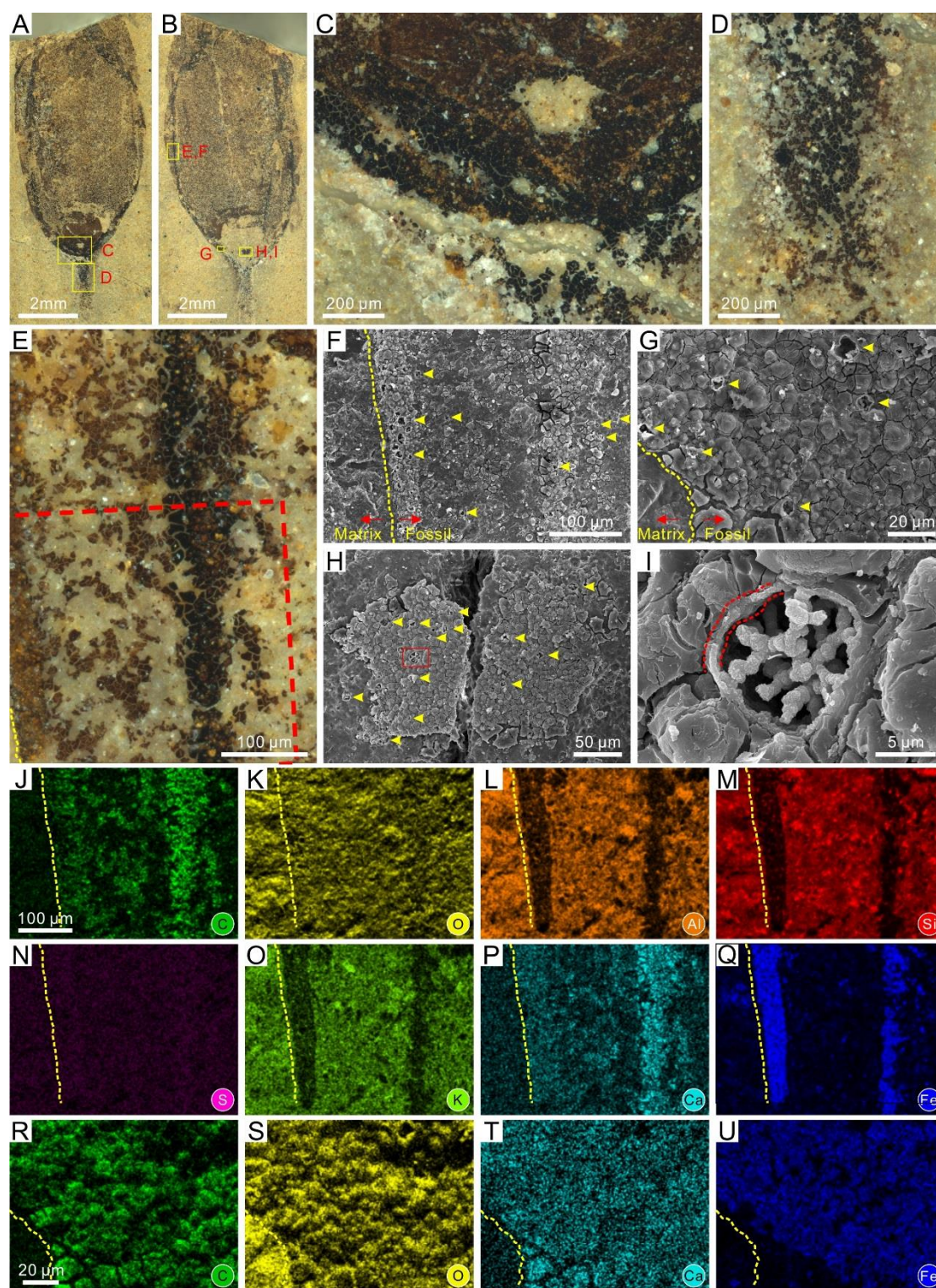


Fig. 5. Photographs, reflected light photomicrographs, SEM images, and EDS
 elemental maps of specimen LTL L0129-1 and specimen LTL L0129-2. (A–B)
 Photographs of *Longfengshania* specimen LTL L0129-1 and its counterpart LTL
 L0129-2. Yellow boxes show the regions examined in (C–I). (C–E) Close-ups of boxed
 area in (A) showing the brown to black carbonaceous patches. (F) SEM image of the

boxed area in (E) showing the carbonaceous patches and the closely associated Fe rich clay minerals. Yellow dashed line corresponds to fossil edge. Arrowheads indicate the void structures. (G–H) SEM images showing the carbonaceous patches and the void structures. Yellow dashed line in (G) corresponds to fossil edge. (I) Close-up of the boxed area in (H) showing a void structure with aggregated rosettes of platelets enclosed by a thick crust. (J–Q) Elemental maps of the same area as in (F) showing the coincidence of C and Ca on the carbonaceous patches. Note that the elemental maps of C and Fe do not share the same distribution, indicating incomplete replacement of the carbonaceous patches by Fe rich clay minerals. (R–U) Elemental maps of the same area as in (G) showing elevated C and Ca abundance on the carbonaceous patches and the incomplete replacement of carbonaceous patches by Fe rich clay minerals.

915

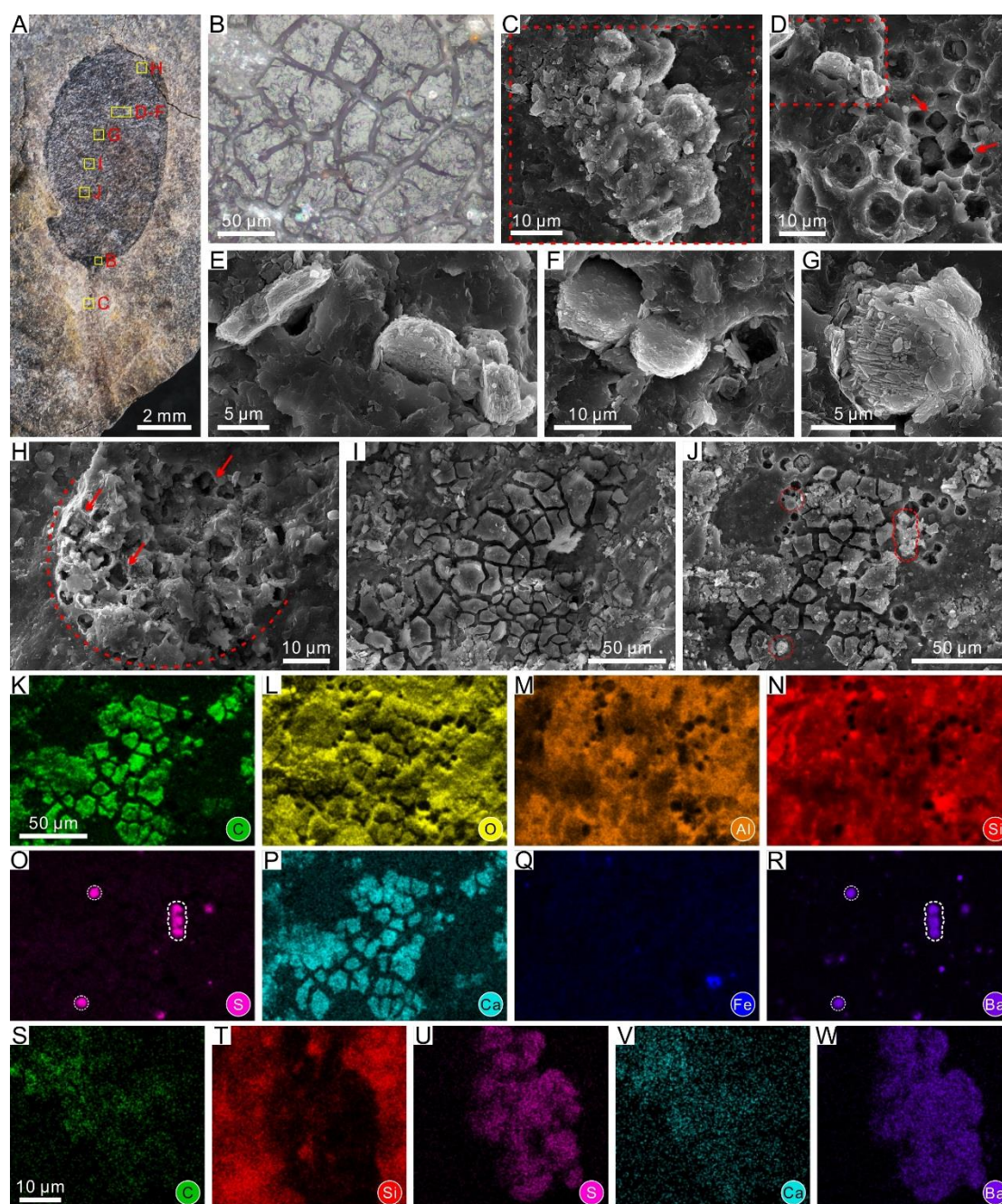


Fig. 6. Photographs, reflected light photomicrographs, SEM images, and EDS elemental maps of specimen LTL L0529. (A) Photograph of *Longfengshania* specimen LTL L0529. Yellow boxes denote the region examined in (B–J). (B) Reflected light photomicrographs showing the black carbonaceous patches. (C–G) SEM images showing the voids, some filled by spherical or tabular barite minerals. Note the molds of dissolved pyrite crystals with straight facets (red arrows) in (D). (E) Enlarged view of the boxed area in (D). (H) SEM image showing framboids which were partly dissolved, some still retaining their euhedral crust but empty inside (red arrows). (I–J)

925 SEM images showing the carbonaceous patches and the voids which are occasionally
926 filled with barite minerals. (K–R) Elemental maps of the same area as in (J) showing
927 elevated C and Ca abundance on the carbonaceous patches. Note the barite minerals
928 filled in the voids (O, R). (S–W) Elemental maps of the boxed area in (C).
929

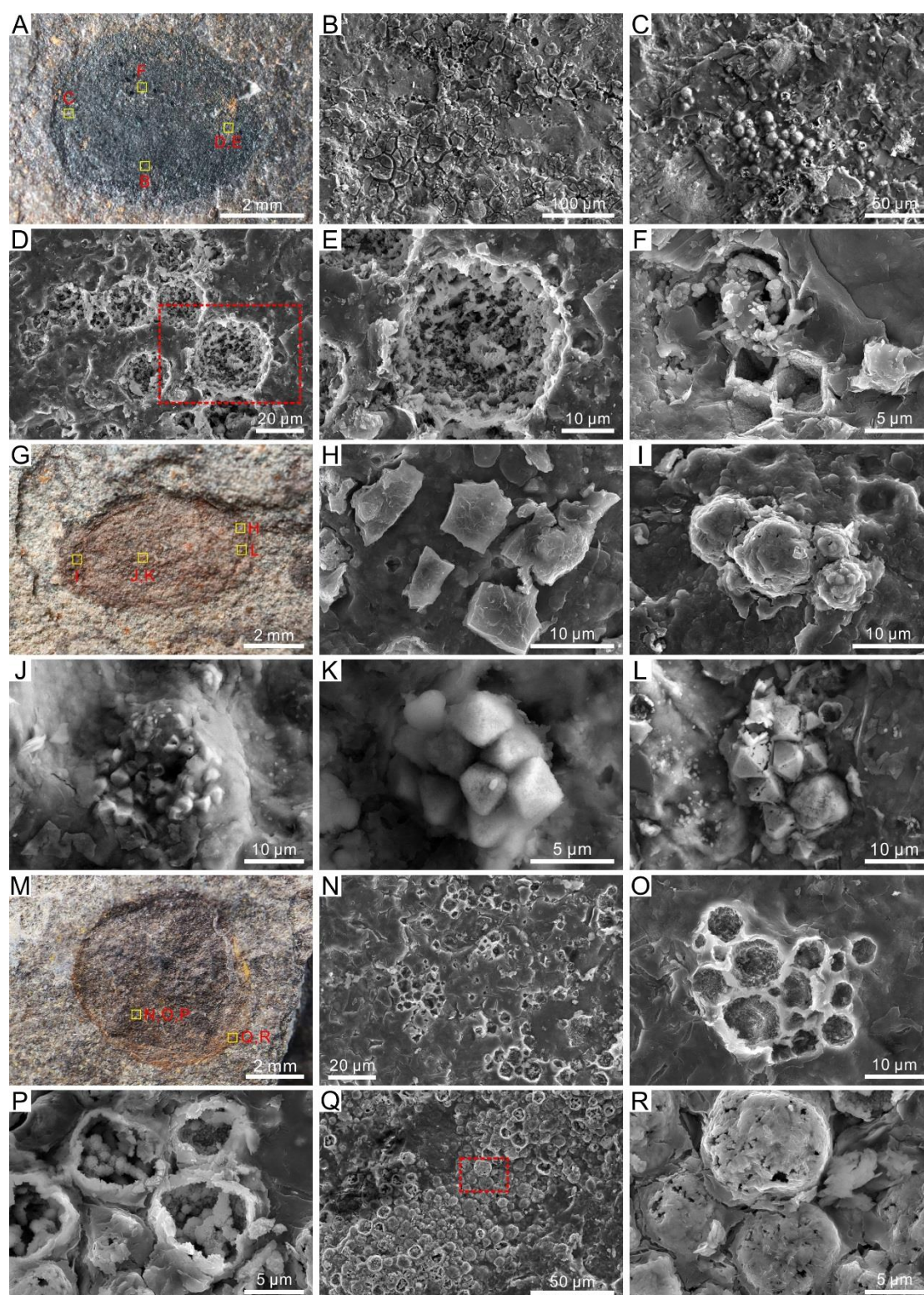


Fig. 7. Photographs and SEM images of *Chuarina* specimen LTL C0586, *Tawuia* specimen LTL T1586, and *Chuarina* specimen LTL C1598. (A) Photograph of unweathered *Chuarina* specimen LTL C0586. (B) SEM image showing the carbonaceous patches and the void structures. (C) SEM image showing carbonaceous patches inlaid

with Fe rich minerals. (D) SEM image showing voids with internal morphology like the cavities formed by removal of pyrite framboids due to weathering. (F) SEM image showing now-hollow euhedral pyrite crystals. (G) Photograph of weathered *Tawuia* specimen LTL T1586. (H) SEM image showing carbonaceous patches. (I) SEM image showing Fe rich clay minerals embedded in carbonaceous patches. (J–L) SEM images showing framboids. (M) Photograph of weathered *Chuaria* specimen LTL C1598. (N–O) SEM images showing the carbonaceous patches and the void structures. (P) SEM image showing aggregated rosettes of platelets enclosed by thick crusts. (Q–R) SEM images showing Fe rich clay minerals embedded in carbonaceous patches. (R) Close-up of boxed area in (Q).

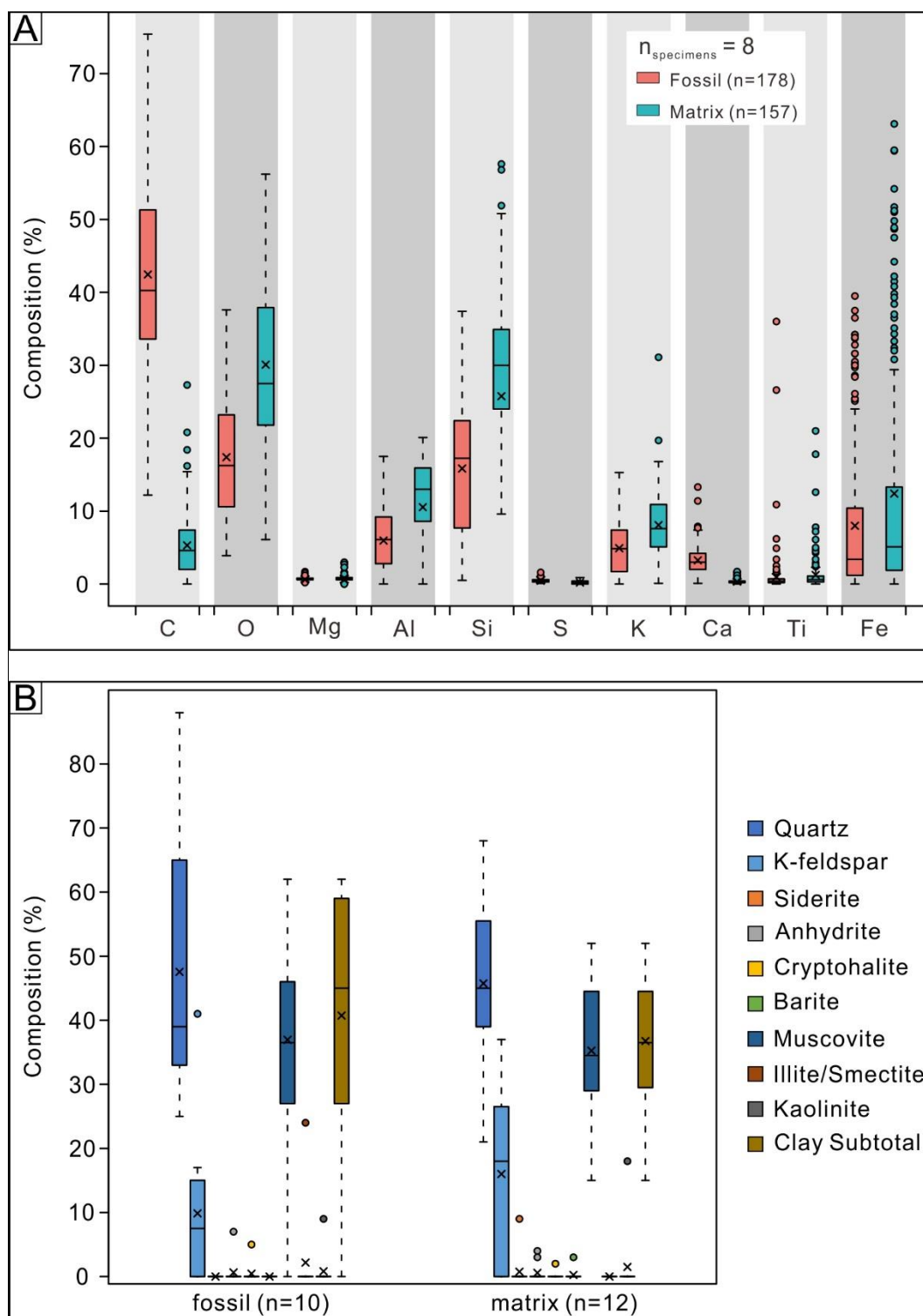


Fig. 8. EDS point analyses and selected-area XRD results. (A) Box plot of the EDS point spectra for the eight analyzed specimens. Note the elevated concentrations of C and Ca, and reduced O, Si, Al, and K concentrations in the fossils relative to the matrices. (B) Box plot of the selected-area XRD data showing the mineral compositions of the fossils and their respective matrices.

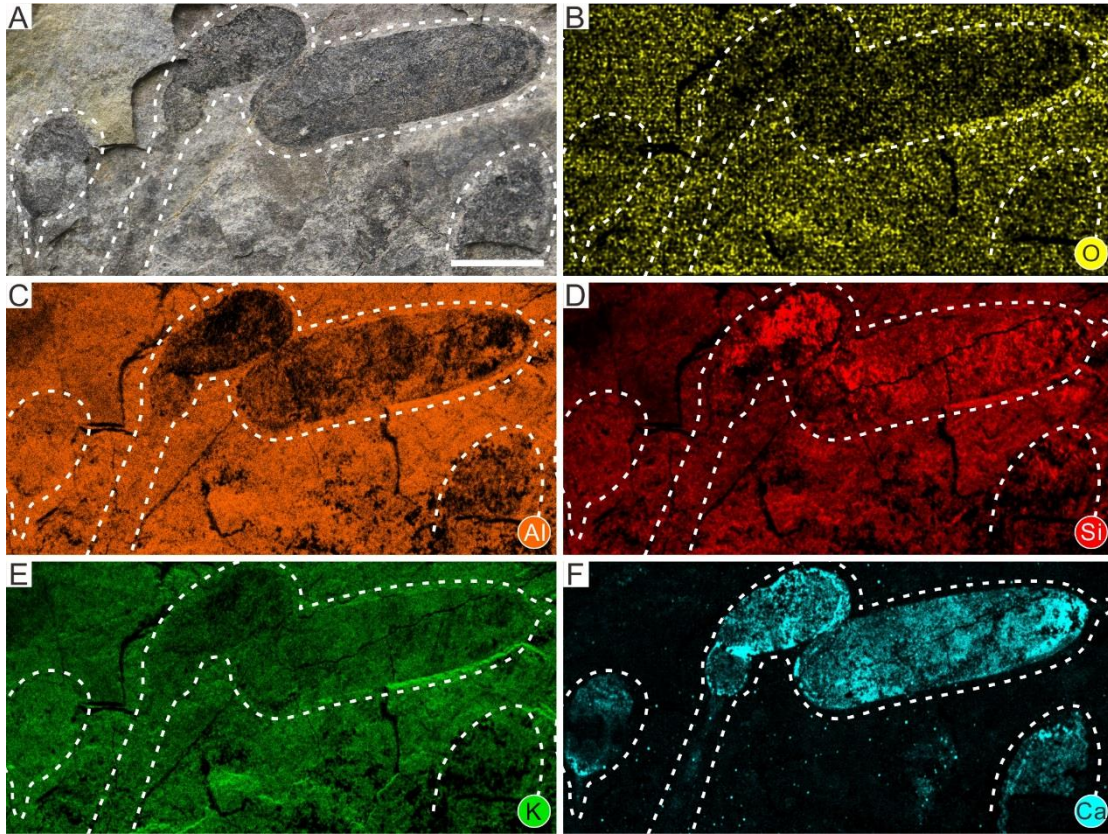


Fig. 9. Photograph and μ -XRF elemental maps of specimen LTL L0429 showing the prominent enrichment of calcium within fossils relative to the surrounding matrix. (A) Photograph of specimen LTL L0429. (B–F) Elemental maps of the same area as in (A) showing the distribution of elements O, Al, Si, K, and Ca. Brightness of color corresponds to abundance of each element. Scale bar in (A) represents 5 mm and the same for (B–F).

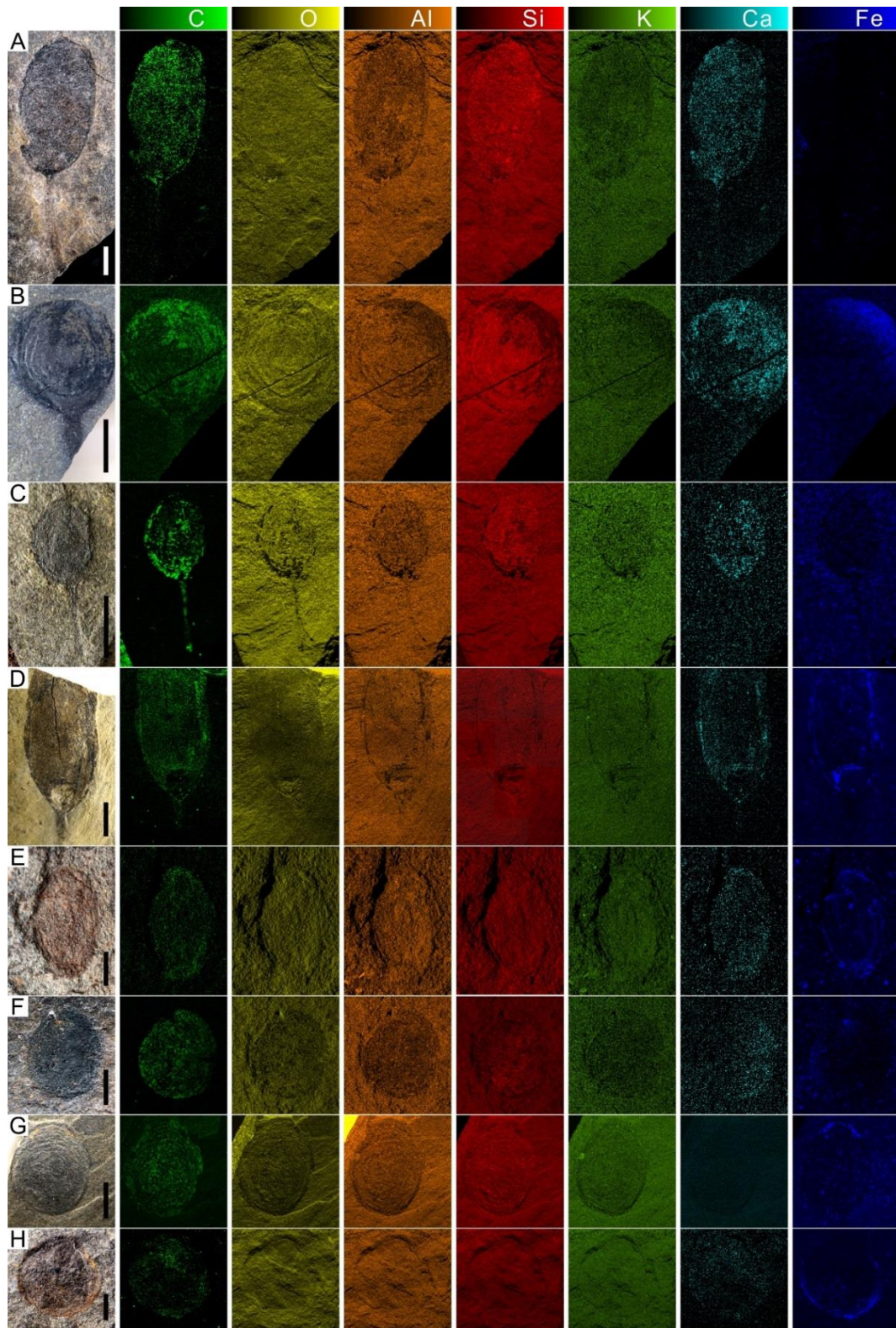


Fig. 10. Photographs and EDS elemental maps of the eight analyzed fossil specimens. All specimens show elevated concentrations of C and Ca, and reduced O, Si, Al, and K concentrations relative to the matrix. Brightness of color corresponds to abundance of each element. Scale bar represents 2 mm in (A–G).

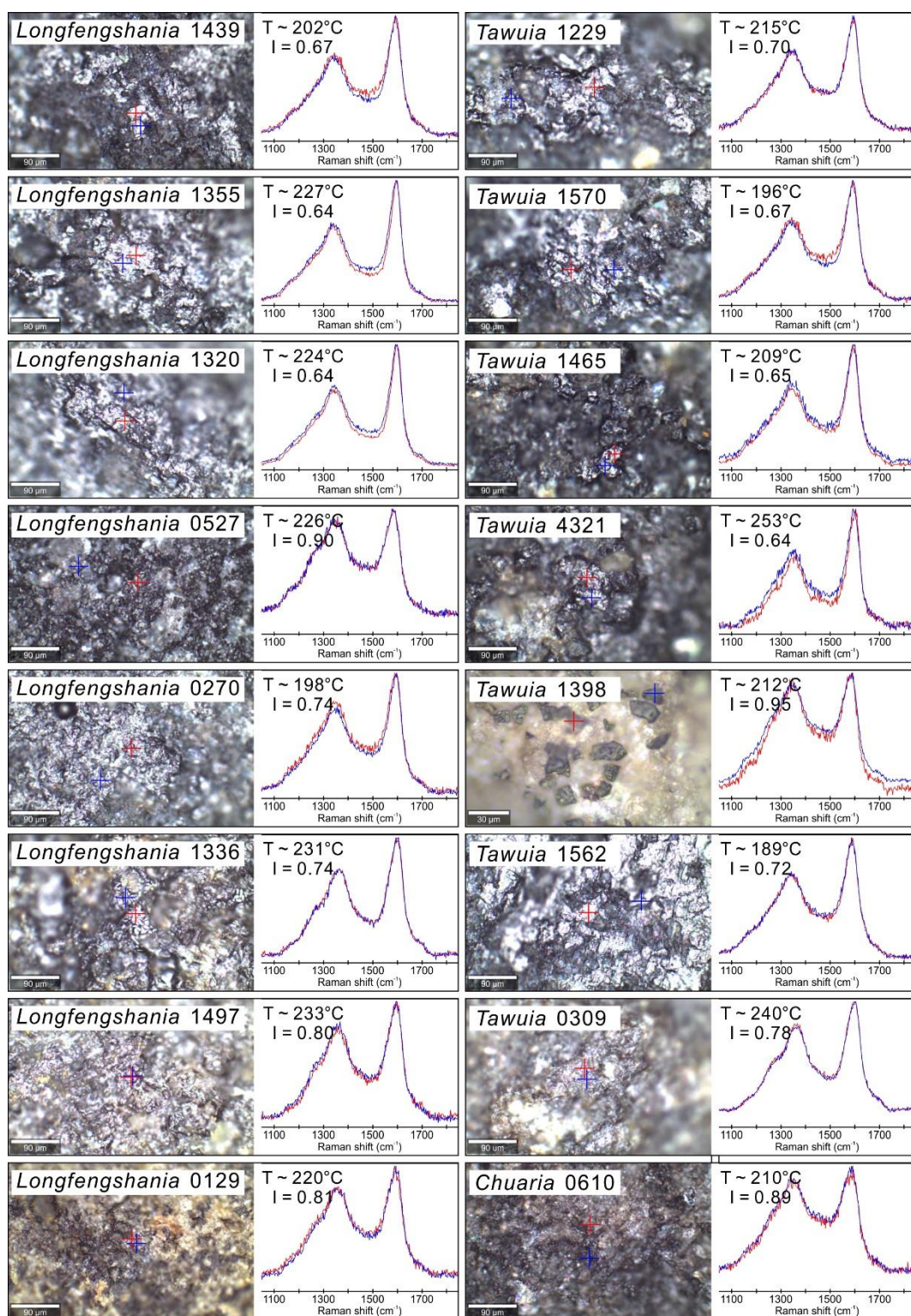


Fig. 11. (A) Reflected light photomicrographs and the confocal laser Raman spectra of the carbonaceous patches of the 16 analyzed fossil specimens. Spectra were probed on the surface of the carbonaceous patches, indicating the carbonaceous nature of fossils. Position of the probed sites are marked by red and blue crosses in reflected light photomicrographs.

971 Table 1. Summary of EDS point spectral data for eight specimens from the Luotuoling Formation. Data for fossils obtained from carbonaceous patches that are
972 macroalgal remains, and for matrix obtained from surrounding host rock with no carbonaceous remains. All elemental point data are reported in normalized
973 weight percentage (nwp). Elements are organized from left to right according to their atomic number.

Fossil ID		C	O	Mg	Al	Si	S	K	Ca	Ti	Fe	Sum
LTL L0358	Fossil (n=25)	33.2	19.9	0.7	7.2	24.5	0.5	6.0	3.0	2.0	2.9	100.0
	Matrix (n=20)	7.4	23.9	0.7	12.8	36.4	0.5	11.4	0.5	0.8	5.7	100.0
LTL L0380	Fossil (n=32)	32.2	14.8	0.8	9.4	22.9	0.7	8.4	4.4	0.7	5.7	100.0
	Matrix (n=16)	8.3	22.9	0.8	14.8	30.2	0.5	12.4	0.4	2.9	6.8	100.0
LTL L0529	Fossil (n=26)	58.2	29.9	1.1	0.9	5.5	0.5	0.4	3.5	0.1	0.1	100.0
	Matrix (n=25)	10.6	45.1	0.7	9.8	28.9	0.3	3.6	0.2	0.3	0.6	100.0
LTL L1497	Fossil (n=15)	45.0	18.3	0.7	7.7	16.3	0.2	5.8	2.1	1.2	2.7	100.0
	Matrix (n=15)	2.2	35.1	0.7	13.3	35.4	0.0	8.7	0.2	0.7	3.7	100.0
LTL T0671	Fossil (n=45)	37.5	12.2	0.7	5.1	12.9	0.3	4.9	3.6	0.9	21.9	100.0
	Matrix (n=45)	3.7	22.6	0.9	8.7	23.0	0.0	6.4	0.5	1.7	32.4	100.0
LTL T1586	Fossil (n=4)	37.1	23.8	0.8	6.4	21.4	0.4	4.5	3.1	0.4	2.4	100.1
	Matrix (n=5)	2.8	35.4	1.0	15.6	32.8	0.2	8.1	0.3	0.9	2.9	100.0
LTL C0217	Fossil (n=15)	41.5	6.6	0.5	9.4	23.4	0.5	7.5	0.2	2.4	8.0	100.0
	Matrix (n=15)	3.5	22.4	0.7	16.6	31.8	0.4	12.4	0.3	1.8	10.1	100.0
LTL C1598	Fossil (n=16)	65.5	20.5	0.7	2.8	4.4	0.7	0.5	4.0	0.2	0.5	99.7
	Matrix (n=16)	1.4	43.4	0.7	15.0	30.3	0.2	6.8	0.2	0.3	1.7	99.9
Average	Fossil (n=178)	43.8	18.3	0.7	6.1	16.4	0.5	4.7	3.0	1.0	5.5	100.0
	Matrix (n=157)	5.0	31.3	0.8	13.3	31.1	0.3	8.7	0.3	1.2	8.0	100.0

974
975
976